



UNIVERSITÀ DEGLI STUDI DI SIENA

FACOLTÀ DI SCIENZE MATEMATICHE, FISICHE E NATURALI
Corso di Laurea Triennale in Fisica e Tecnologie Avanzate

TESI DI LAUREA
18 Aprile 2011

A Large GEM detector prototype

Test-beam results and analysis

Candidato:
Elena Graverini

Relatore:
Prof. Nicola Turini

Abstract

My thesis presents the characterization of a new Gas Electron Multiplier detector prototype. The tests were performed at CERN laboratories, in Genève, and aimed at checking the prototype efficiency when working in high-radiation environments similar to the ones which it was designed to work in, the LHC (Large Hadron Collider).

The manufacture of the detector is described, with its distinctive features; the preliminary tests on the components; the data acquisition electronics; the test beam setup; and lastly the test beam extracted data.

My thesis will also go through the data analysis procedure, presenting some of the routines that were written for this purpose; the achieved results will be shown and commented, focusing on the differences between the prototype and a "common" GEM detector and pointing out opportunities for further improvements.

Sommario

La mia tesi presenta la serie di test eseguiti su un nuovo prototipo di rivelatore di particelle di tipo Gas Electron Multiplier. Si tratta di un rivelatore di grande area realizzato con una tecnica che permette di unire più fogli GEM di dimensioni minori in un solo piano e di evitare problemi di allineamento in fase di foratura.

I test sono stati eseguiti nei laboratori del CERN di Ginevra allo scopo di verificare le prestazioni del prototipo e la sua resistenza in ambienti ad alto contenuto di radiazioni: questa nuova tipologia di rivelatori è stata infatti disegnata per un futuro utilizzo in LHC (Large Hadron Collider).

Esporrò in dettaglio il processo di costruzione del prototipo, i test preliminari di guadagno e l'analisi del rumore; verrà descritta l'elettronica di readout, per poi passare all'allestimento del periodo di test su fascio di particelle; esaminerò i risultati ottenuti nell'ottica di un'integrale caratterizzazione del rivelatore. Mostrerò alcuni degli algoritmi utilizzati per l'analisi dei dati raccolti durante il test beam.

I risultati ottenuti verranno infine esposti illustrando le differenze con le prestazioni dei rivelatori a tecnologia GEM di dimensioni standard, e suggerendo le migliorie che possono ancora essere apportate.

Contents

1	Large GEM prototype and test setup	9
1.1	GEM detectors	9
1.2	A large triple GEM detector	11
1.3	Electronics	13
1.3.1	VFAT readout chip	13
1.3.2	Turbo readout card	17
1.4	Experimental setup	17
1.4.1	Test beam	17
1.4.2	The telescope	18
1.5	Data analysis system	20
1.5.1	Hits, clusters and tracks	20
1.5.2	Beam profile reconstruction	21
2	Off beam analysis	25
2.1	Large GEM characterization	25
2.1.1	Gain curve	25
2.1.2	Gas mixtures	27
2.2	Noise	27
2.2.1	Off beam threshold scan	27
3	On beam analysis	29
3.1	Efficiency of the tracker	29

3.2	High voltage scan	30
3.3	Threshold scan	33
3.4	Timing scan	37
3.5	Behaviour with hadron beam	44
4	Remarks	47
4.1	(In)homogeneity of the prototype	47
4.1.1	Chamber borders, spacer frame and foils junction zone	47
4.1.2	Effects of the different dimensions of the pads	51
4.2	Data analysis system efficiency	54
4.2.1	Efficiency radius	54
4.2.2	Cuts	58
5	Conclusions	61
5.1	Quality of the large GEM prototype	61
5.2	Large GEM detectors in TOTEM and CMS experiments . . .	62
	Appendix A ROOT analysis routines	67
	Bibliography	73

Large GEM prototype and test setup

1.1 GEM detectors

High-energy physics experiments aim at detecting the presence and characteristics of particles. Different kinds of detectors are used in order to achieve this, which can reveal different features of the particle itself: kinetic energy, momentum, charge, mass and even its internal structure.

Gas ionization detectors can reveal high-rate electromagnetically-interacting particles. If the incident photon or massive charged particle has enough energy to ionize one atom of gas inside the detector, the ion-electron pair flux will generate a current pulse for each event which can be separately revealed by some conducting material structure and then can be sent to any electronic *data acquisition* (DAQ) setup.

Depending on the voltage applied, gaseous detectors can produce an avalanche multiplication of the signal by accelerating the first electrons produced by the incident particle and causing them to create more pairs. Gas electron multipliers (*GEMs*) are based on this principle. *GEM foils* consist of two thin copper layers, with a kapton foil between them. Small and regular holes are produced through copper and kapton foils, via chemical processes such as photolithography and acid etching. High voltage is then

applied between the two copper foils (*anode* and *cathode*) to put the GEM foil in operation; this will create a high electric field through the holes:

$$E = \frac{V}{d}$$

where E is the electric field, V is the voltage and d is the distance between anode and cathode. Since the kapton foil is very thin, but the voltage applied can be high¹, the electric field inside the GEM holes can be as high as

Typically a GEM-based detector consists of one or more GEM foils inserted between a copper foil (*cathode*) and a readout plane (*anode*):

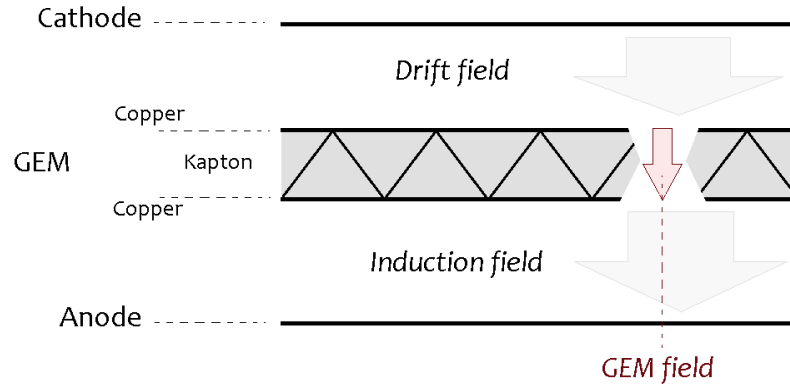


Figure 1.1: Schematics of a GEM-based detector (single GEM foil)

The different detector layers require different voltage settings: a *drift voltage* to guide electrons from the cathode drift foil to the GEM, an *amplification voltage* between the copper layers of every GEM foil, and an *induction voltage* to guide electrons from the GEM bottom layer to the readout plane.

¹Kapton is a plastic polyimide designed so that its molecular structure remains stable in a wide range of temperatures. It was found to be highly radiation-hard, and is commonly used for its good insulating characteristics.

1.2 A large triple GEM detector

Using $66 \times 66 \text{ cm}^2$ GEM foils, a prototype triple GEM detector with an active area of about 2000 cm^2 was built [10]. Two innovative techniques were used to manufacture this detector: *single-mask* etching and *GEM foils splicing*.

GEM foils are produced by the same photolithographic processes as for building common printed circuit boards. Typically, small GEMs are etched on both sides to produce symmetric holes; however, it is very uncomfortable to align masks when the GEM foil dimensions grow. In the case of this large area prototype, it was virtually mandatory to develop a single-mask etching technique. As shown in Figure 1.2, after the top copper layer is etched, the holes in the polyimide material (Kapton) are made by a basic mixture containing potassium hydroxide (KOH, which etches isotropically) and ethylene diamine ($\text{C}_2\text{H}_4(\text{NH}_2)_2$, which etches anisotropically). An anisotropic etcher is needed to keep the holes aspect ratio, defined as $\frac{\text{depth}}{\text{width}}$, high.

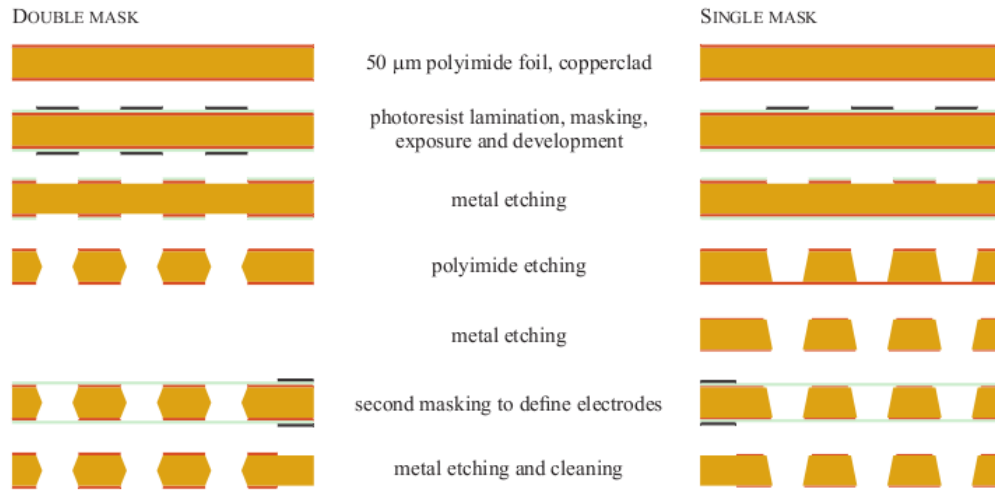
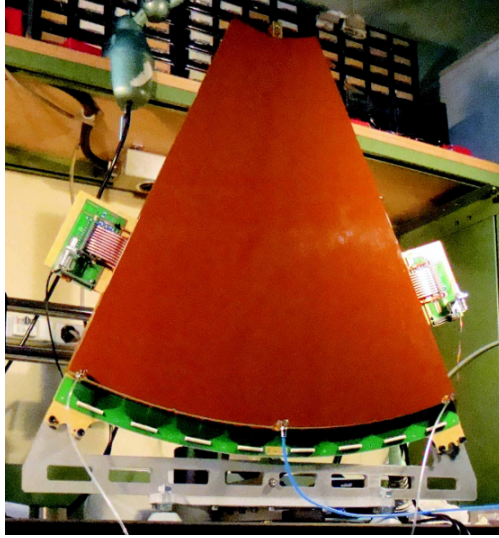


Figure 1.2: Comparison of the standard *double-mask* and the new *single-mask* GEM etching procedures

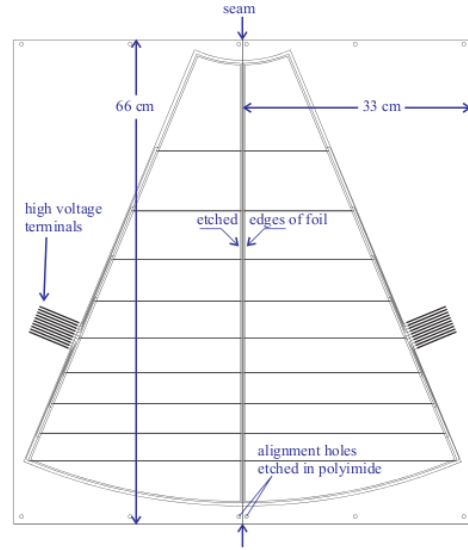
The bottom copper layer is then etched from both sides, using the holes in the kapton as mask, dipping the whole foil in an acidic etchant mixture in

order to finalize the holes and to slim the electrodes thickness.

Suppliers of the base material to produce GEM foils can so far offer only around half a meter wide rolls. Two crosswise halves of a $66 \times 66 \text{ cm}^2$ foil were spliced together by covering the junction with a $25 \mu\text{m}$ Kapton adhesive substrate. The glue polymerized after a baking. Rate capability tests demonstrated how the the performance of the chamber remains unaffected except for the 2 mm wide seam zone [9]. In addition, for the triple GEM detector we tested a $0,5 \text{ cm}$ wide plastic spacer placed within the chamber totally covered the junction area, making it impossible to recognize the specific loss of efficiency due to the seam.



(a) View of the prototype

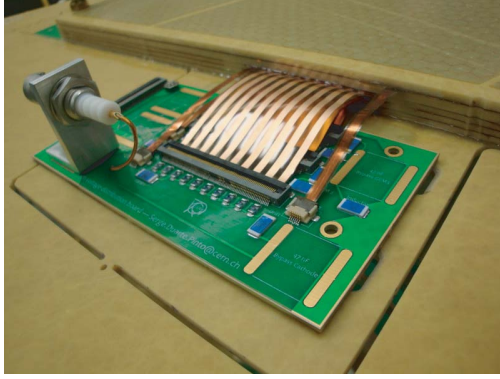


(b) Layout of the GEM foils sectors

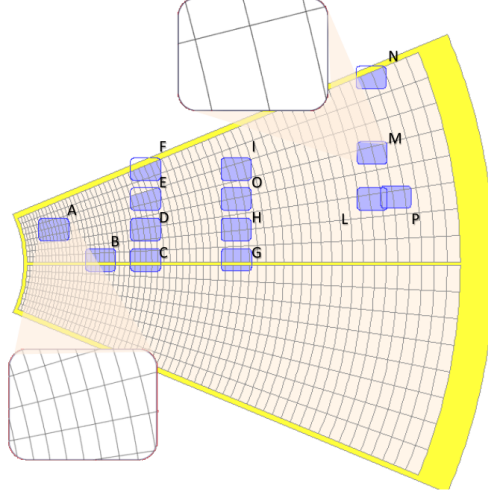
Figure 1.3: Schematics of the large area triple GEM detector

To reduce the discharge probability the cathode electrodes are segmented and connected to the power supply via $10 \text{ M}\Omega$ resistors. For the high voltage distribution a compact divider board was used, making it easy to eventually debug the circuit. Since it was not planned to handle such high voltages, groups of pins were connected together and alternated with groups of floating

strips (see Figure 1.4(a)).



(a) Divider board



(b) Readout plane, made of pads

Figure 1.4: A view of the compact divider board, and the schematics of the pad-based readout with indication of the beam-tested regions

The readout configuration consists of 1024 pads, each with a surface that goes from $0,25\text{cm}^2$ (in the narrower part of the detector) to 6cm^2 . Figure 1.4(b) shows the differences in dimension within the readout pads; the image also points out the zones where we directed the beam during the test of the chamber.

The readout VFAT chips were connected to the detector via small hybrid printed circuit boards, which were bound to the detector itself on its larger rounded border.

1.3 Electronics

1.3.1 VFAT readout chip

VFAT2 is the front-end ASIC (*Application Specific Integrated Circuit* in use at the TOTEM experiment in LHC. It converts the signal from the detectors

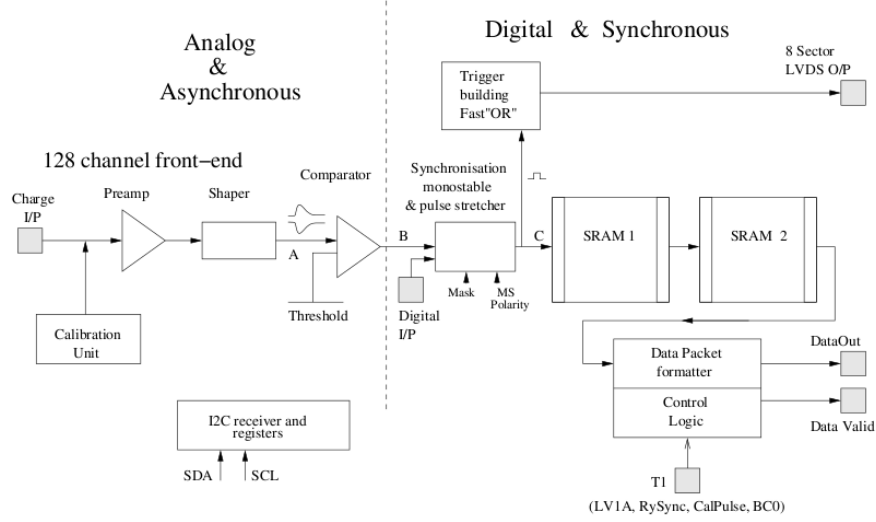


Figure 1.5: Schematics of the VFAT chip [3]

into digital data via an amplifier - shaper - comparator chain.

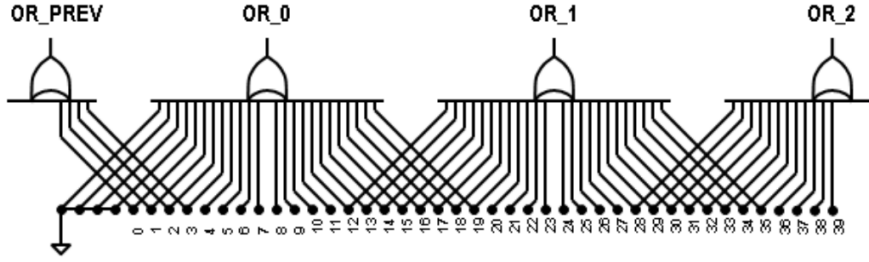
The readout chips used for these test have been **VFAT2** chips as well, since an aim of the test was a compatibility check between large pad based GEM detectors and TOTEM electronics.

VFAT2 features a *transimpedance* preamplification step ($V_{OUT} \propto I_{IN}$), whose output is sent to a shaper, and then compared to a programmable threshold potential. The latter is programmable for each channel (*Trim-DAC*) in terms of *VFAT2 DAC step bins*².

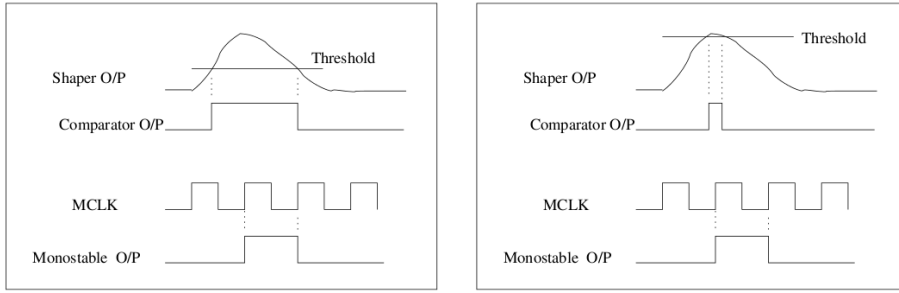
Comparator's output is then made synchronous by the monostable block, which provides by default a $1clk$ pulse.

A *Fast-OR* logic provides in just one clock cycle an **OR** of all channels monostable outputs. This *S-Bit* can then be used as a trigger, to check the

²A *VFAT2 DAC step bin* is defined as the amplitude of a preamplified and shaped signal coming from a number n of electrons produced in the first stage of the detector (the *drift* region), with $n \simeq 460$ to $600 e^-$. It has been however found that, for GEM based detectors, $n \simeq 800 e^-$, and each VFAT2 DAC step bin corresponds to a charge of $0,045fC \approx 3,3mV$.



(a) Fast-OR logic combining the monostable outputs to provide a trigger signal within one clock cycle [2]



(b) Signal shaping for $MSPL = 1clk$ [4]

Figure 1.6: Fast trigger and shaping features of VFAT2 chips

speed of response of the chip and to coordinate the data acquisition.

Monostable settings

The time distribution of charge of a signal can be either thin or large (*time-walk* effect); the preamplifier stage preserves its width. The monostable block allows stretching for its output pulse, which can be programmed to be as long as 1 to 8 clock periods: this generally decreases the time performance, as a subsequent signal may cross the threshold while the monostable output is still high, resulting in a pulse which will go down n clock cycles later.

Stretching the monostable pulse allows however to find whether two or more pulses are to be recognized as originated by the same event. Two effects may indeed happen, that are lightened by the stretching of the monostable output:

Timewalk: adjacent channels may be hit with different intensity (e.g. an electronic avalanche falls over two adjacent pads), causing the least hit to cross the threshold later than those which collected more charge;

Jitter: primary pairs may be release anywhere in the drift region, which has a not-negligible thickness ($\sim 60ns$). Electrons produced at different heights won't reach the anode at the same instant, while they have been produced by the same incident particle.

Threshold

Setting a threshold is needed to prevent undesired hits (e.g. noise) to affect our data sets. VFAT2 allows setting both positive and negative thresholds, by changing the values of two registers as shown in Table 1.1 [4].

Positive threshold	$V_{T1} = 0$	$V_{T2} = \text{variable}$
Negative threshold	$V_{T1} = \text{variable}$	$V_{T2} = 0$

Table 1.1: Threshold setting in VFAT2

The most of our scans were run at $th = -60ds$ (where i call ds a *VFAT2 DAC step bin*). Threshold scans were performed as well, to see at what level the noise starts to become relevant with respect of the real signal: see Chapter 3.3 on page 33.

The typical threshold-crossing time spread of GEM detectors is around $\sim 70ns$, because of the variety of shapes that signals can have when detecting minimum interacting particles such as fast muons, producing *jitter* and *timewalk* effects.

Latency

Given a trigger signal, we define **latency** the number of SRAM slots the chip has to go back to read the digital output of the event corresponding to that trigger. It is measured in clock periods, as it represent in some way the speed of the detector-readout system: The larger is its latency, the

faster is the detector's response; subsequent delays are raised by the readout electronics.

The latency of our setup was found to be $lat = 17clk$ when working with Ar/CO₂ 70/30, and $lat = 18clk$ when working with Ar/CO₂/CF₄ 60/20/20.

1.3.2 Turbo readout card

1.4 Experimental setup

1.4.1 Test beam

CERN provides researches with **test beam** facilities to check detectors before letting them down into the LHC cavern. Our trial period was scheduled between 12th and 22th August, 2010, and it took place at the **H4** beam line in Prévessin.

Bunches of protons are accelerated in the SPS, a circular particle accelerator, to a momentum of about $450GeV/c$; the beam is then branched into several channels, each of them terminating in a target where the incident protons create secondary particles. In our case, the target (**T2**) produced pions π^- , with a momentum of $150GeV/c$. These straight beam lines lie in the site of Prévessin; the beam is divided into several branches in order to provide more than one permanent or temporary test beam facility at a time.

Both hadron and lepton beams are provided, so that all the possible test requests made by the various experiments are covered. Pions have a mean lifetime $\tau = (2,6033 \pm 0,0005) * 10^{-8}s$; their primary decay branch (with *branching ratio* $\Gamma_i/\Gamma = (99,98770 \pm 0,00004)\%$ [1]) is leptonic:

$$\pi^- \longrightarrow \mu^- + \bar{\nu}_\mu$$

H4 beam is made of both pions and their decay products, muons. Switching to a pure lepton beam is possible closing the beam collimators: at this energy muons are minimum interacting particles (**MIPs**) and pass through

the collimators, while pions are stopped. A muon beam is wider than a pion one.

We tested the large prototype GEM detector on:

- a $0,8kHz$ μ^- beam;
- a $38kHz$ π^- beam;
- several π^- beams at intermediate intensities, in order to check if there were possibilities of experiencing charging up effects.

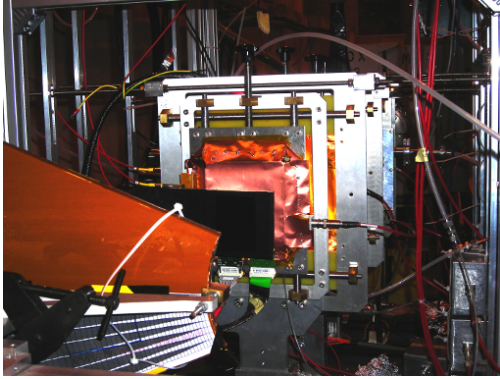
1.4.2 The telescope

The test-beam experimental setup was conceived so that it made use of the RD51-GDD³ tracker. The tracker is made of:

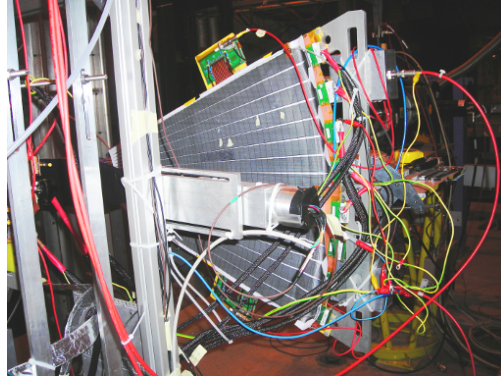
- 3 scintillators, used as a trigger;
- 3 $10cm \times 10cm$ GEM detectors, used as a track detecting system;
- a metallic frame to support the tracker together with the detector prototypes (one or more) that are to be tested.

All the cables, the dividers and the cards were also fixed to the metallic frame, which was aligned so that the detectors were perpendicular to the beam line. Figure 1.7 on the next page shows the final setup. The signals from the scintillators were sent to three comparators connected to an **AND** port, the output signal of which was used as **trigger**. The trigger signal was sent to the *turbo₀* card, which acted as master and forwarded that signal to itself (on another input pin) and to the slave card *turbo₁*. The two *turbo* cards controlled and received inputs from the *VFAT* chips (both those on the tracking GEM detectors and those on the LG prototype), which collect and preamplify the detected signals.

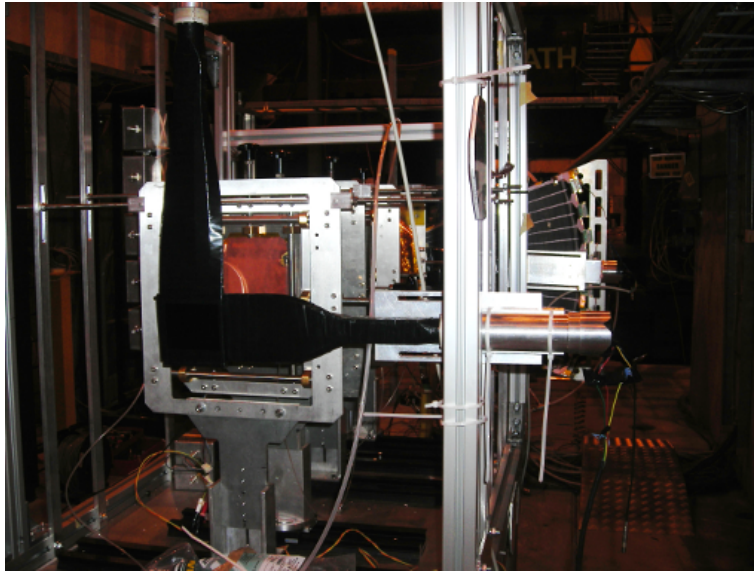
³The abbreviations stand for the CERN *Research and Development* group no. 51, and the *Gas Detector Development* group



(a) Tracker system setup



(b) Large GEM prototype setup



(c) View of the telescope

Figure 1.7: The test-beam experimental setup: a telescope made of scintillators, small GEM tracking chambers, and the Large GEM prototype

DAQ chain

1.5 Data analysis system

1.5.1 Hits, clusters and tracks

A **hit** on a detector occurs when one of its readout channels collects enough charge to exceed the threshold set in the readout chip. This happens when a particle has produced an avalanche in the multiplication area of the detector, but noise and *cross-talk* between adjacent readout channels can also produce a moderate number of hits.

We define **cluster** a set of adjacent hitted channels along the x or y axis. A one-channel wide gap is allowed within the set. To make the test simpler, the tracks of the incident particles were only reconstructed if:

1. all of the tracker chambers showed one and only one cluster along the x axis;
2. the hit number in all the tracker chambers was ≤ 120 .

The track reconstructing algorithm exploits ROOT's class *TGraphErrors*. The distance along the z axis between the tracker chambers is measured; the x position of clusters is plotted versus z in a *TGraphErrors* object, and fitted with a first order polynomial via the ROOT *Fit()* function. This way, the fit function itself and its parameters (χ^2 , residuals, q and m) become available into the x -track object itself. The same procedure is used to define y -track objects.

If we define n_{act} as the number of actual hits and n_{exp} as the number of expected hits, then

$$\frac{n_{\text{act}}}{n_{\text{exp}}}$$

is the Large GEM's **efficiency**. n_{act} is incremented, and a simple histogram is updated, every time that the distance between the hit on the LG and the

projection on the LG of the corresponding track is minor than an assigned *efficiency radius*.

1.5.2 Beam profile reconstruction

A first check on the DAQ chain and the data analysis system efficiency was done by reconstructing the beam profile (which was known) from the tracker and LG data. Figure 1.8 on the following page shows our first attempt at it:

1. we set a cut on the data: we requested that $\chi^2 < 10$ for every track, in both x and y directions, and low residuals for the hit positions ($\Delta x < 10channels$ and $\Delta y < 10channels$);
2. we plotted the position of the x clusters detected by the first tracker chamber (the *zero* is set at the lower left corner of it; since the strip pitch is $0.4mm$ the position is computed by making $0.4 * pos_{CL}$, where pos_{CL} is the position of the cluster expressed in channels number);
3. we plotted the hits on the LG channels to detect the most irradiated ones;
4. we plotted again the position of the x clusters detected by the first tracker chamber, each time requesting that the hit LG channel was one of the previously found ones.

This way we made a sort of puzzle which pieces represent the beam portion seen by one of the LG channels. It is like projecting the shadow of the LG pad corresponding to that channel on the tracker beam profile reconstruction.

We can see on Figure 1.8 on the next page that the LG pads fairly detected the beam profile. The difference in height of the two profiles (that from the tracker and that from the LG) is due to the fact that we did not include in the plot some of the adjacent LG channels, which indeed caught a little part of the beam.

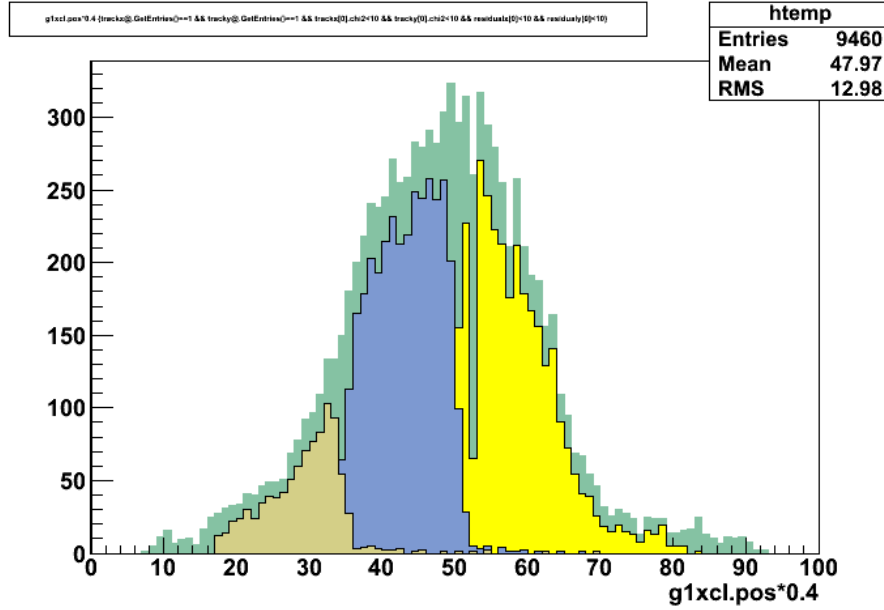


Figure 1.8: LG channels 699, 700 and 701 beam x profile reconstruction. The green background area is the beam x profile as seen by the first tracker chamber.

A two-dimensional plot can be done as well. A `GetX()` and a `GetY()` functions were defined to extract x and y pad position informations from the number of the corresponding LG channel. Figure 1.9 on the facing page shows the two-dimensional distribution of the hits gathered by the prototype, in linear and logarithmic scales, as well as the tracker profiles for comparison.

The beam shown in Figure 1.9 on the next page is a muons beam, and thus it is quite large in both directions. When we dealt with a pions beam, it was sharper and 4 adjacent pads on the LG were enough to collect almost all the signal.

The beam profile reconstruction algorithm seems to work well, and so does the track reconstruction one.

Figure 1.9(b) on the facing page gives an idea of the noise affecting the prototype: some channels look like hitted while the beam was located in another area. Anyway, the scale of the plot is logarithmic, and in this case

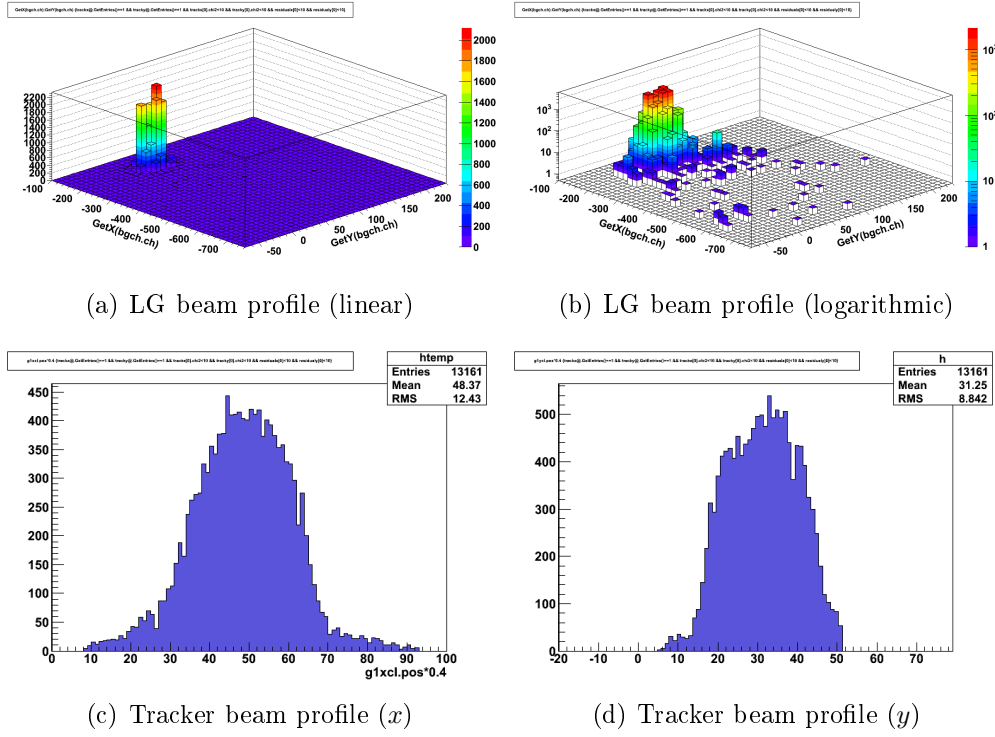


Figure 1.9: Two-dimensional beam profile reconstruction

the noise intensity is really negligible in respect to that of the beam.

Chapter 2

Off beam analysis

2.1 Large GEM characterization

2.1.1 Gain curve

Before the scheduled test beam period, Serge Duarte Pinto¹ had performed a study on the gain of the prototype, using Ar/CO₂ 70/30 gas mixture and Cu X-Rays.

The detector gain is the ratio between its output and input currents, that is:

$$G = \frac{I_{out}}{q * f}$$

where q is the charge collected by the first layer of the detector. In this setup q can be computed as:

$$q = n * e$$

where e is the electron charge and n is the average number of electrons produced in the drift region by the incident photon or particle; f is the interaction rate of the incident particles in the gas. Since the energies of the characteristic X-ray lines of the source, and the ionization energy of the GEM gas mixture are known, n is well determined. In this setup (Ar/CO₂ 70/30)

¹CERN researcher, on behalf of RD51 group

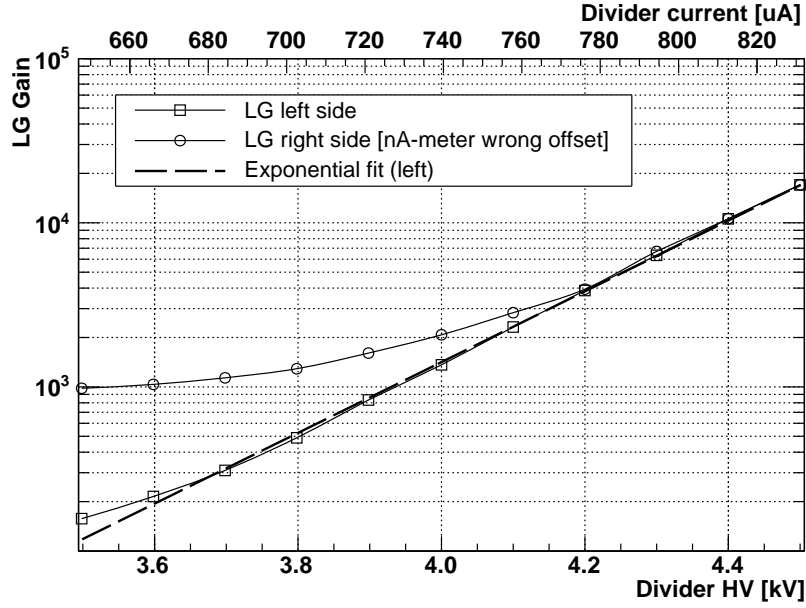


Figure 2.1: Cu X-Ray gain curve for the large prototype GEM detector (S. D. Pinto)

we have $n \simeq 320$.

After q is computed, one needs to measure I_{out} and f in order to obtain G . A measure f is performed by sending the LG output signals first to an amplifier, then to a comparator, and at last to a counter. Connecting together all the 128 pads of the readout line, one can measure I_{out} by an amperometer.

Figure 2.1 shows the results of S. D. Pinto measurements. There are two different plots for the two sides of the chamber, which are separated in voltage supply; the graphs are not symmetric because of a wrong offset of one of the amperometers, which becomes relevant at low current levels. However, the high-gain part of the two graphs coincide, and are well fitted by an exponential function, as one should expect for a GEM detector.

At the test beam we raised the current over $830\mu A$, where Pinto's data

end, losing the possibility to check the exact gain we were getting in the detector. We got to such high voltage values in order to test the prototype with a different gas mixture (see Chapter 3.2 on page 30 and following).

For this and other reasons, a new gain curve is required, which will touch high divider current values and will check the homogeneity of the detector within its left and right sides.

2.1.2 Gas mixtures

2.2 Noise

2.2.1 Off beam threshold scan

A noise measurement was performed in the form of threshold scan, interacting with a *turbo* card to control VFAT chips. A LabVIEW tool was programmed by Eraldo Oliveri² for this purpose.

Threshold scans were performed for all channels of the VFAT chips connected to the large GEM detector. We found some disconnected channels and some noisy ones, but generally the ground layer enclosing the chips worked well in reducing the noise: most of the channels were found to show noise levels similar to those visible in Figure 2.2 on the next page. This means that a threshold $th \geq 35$ VFAT DAC step bins should cut off all of the noise. Indeed, subsequent on-beam results confirmed low noise levels at threshold 40. The reason for few noise hits showing up at that threshold level during the test beam, and not showing at all off the beam, is to be found in the fact that the high voltage was turned on.

More noise analysis have been done by acquiring **S-Curves**: further explanations are in Chapter 4.1.2 on page 51.

²University of Siena - INFN Pisa

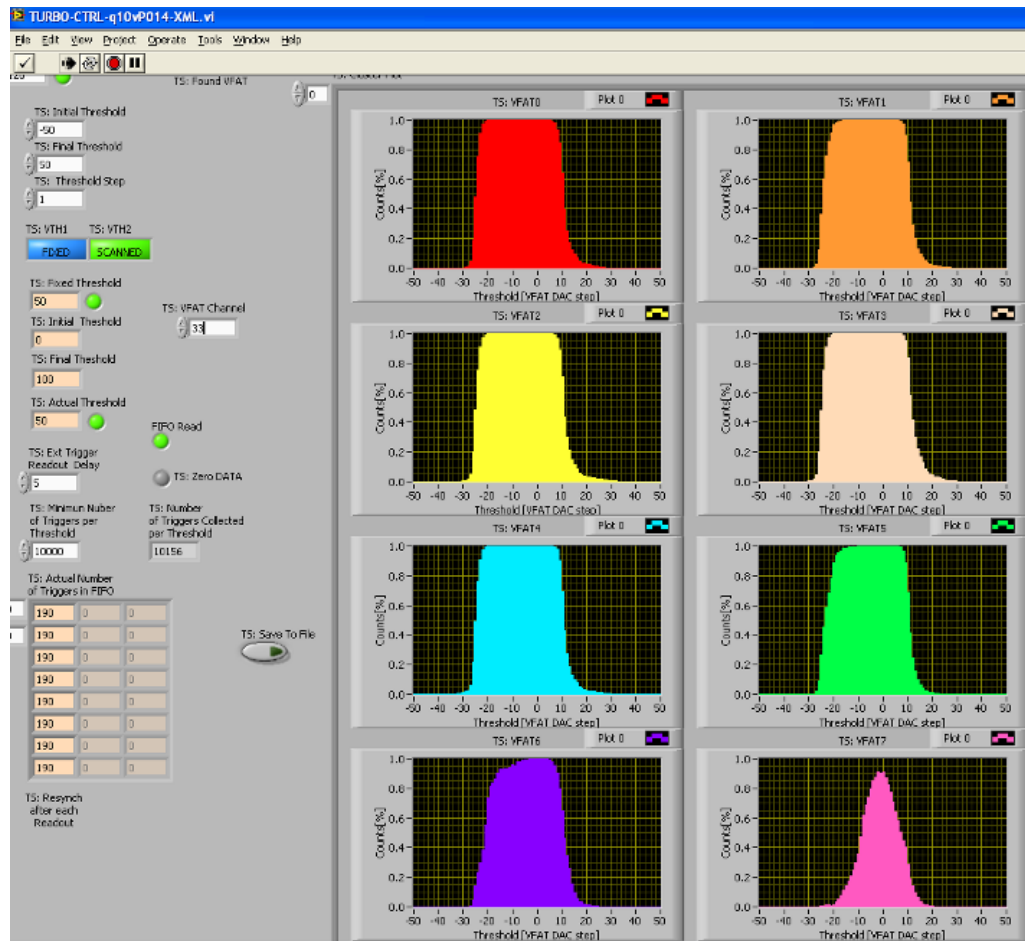


Figure 2.2: An off-beam threshold scan for VFAT channels

Chapter 3

On beam analysis

During the test beam we worked at higher gain than those by S. D. Pinto presented in Chapter 2.1.1 on page 25. Table 3.1 on the following page shows the extrapolated gain values for our working points, using Pinto's exponential fit of his X-Rays gain curve:

$$G = 2 \cdot 10^{-6} e^{0,026 \cdot I}$$

Expected current values refer to both the detector sides; actually, the two presented slightly different amperage, in the range of $I_{left} = (I_{right} \pm \xi) \mu A$, where $0 \leq \xi \leq 4,3$.

3.1 Efficiency of the tracker

At the beginning of the test beam we first checked whether the tracker system was working suitably. We preliminary computed its efficiency without checking if the clusters were corresponding to actual tracks, as we used to for the prototype under test.

The relation between efficiency and threshold, and the one between the average size of clusters and the threshold were computed; a quick latency scan was run. Figure 3.1 on page 31 shows the results.

Divider HV (V)	Expected I (μA)	Expected Gain
-4.600	-764, 8	1.930
-4.700	-781, 5	3.021
-4.800	-798, 2	4.767
-4.900	-815, 1	7.403
-5.000	-831, 3	11.684
-5.050	-840, 1	15.100
-5.100	-847, 9	18.439
-5.150	-856, 7	22.947
-5.200	-865, 1	29.737
-5.250	-873, 4	37.206
-5.300	-881, 4	45.599
-5.350	-890, 2	57.104

Table 3.1: Extrapolated gain values for $I > 750\mu A$

3.2 High voltage scan

Prototype efficiency was first detected as a function of the High-Voltage (subsequently referred to as **HV**) applied on the divider poles. These scans were performed focusing the muon beam on two regions of the chamber (P and A , whose readout plane areas are covered respectively with large and small pads), obtaining slightly different results. This was done to check the LG homogeneity, since it is a large area detector.

The gas mixture inside the detector was Ar/CO₂ in 70/30 proportions.

Four different thresholds were applied, in order to have a complete set of data to be used as reference for future comparison: -40 DAC steps (subsequently called ds), $-60ds$, $-80ds$ and $-100ds$. The length of the monostable pulse (subsequently referred to as **MSPL**) was set at 4 clock cycles (clk) to detect the signal as well as possible; in *point A* we also repeated the scan setting $MSPL = 3clk$.

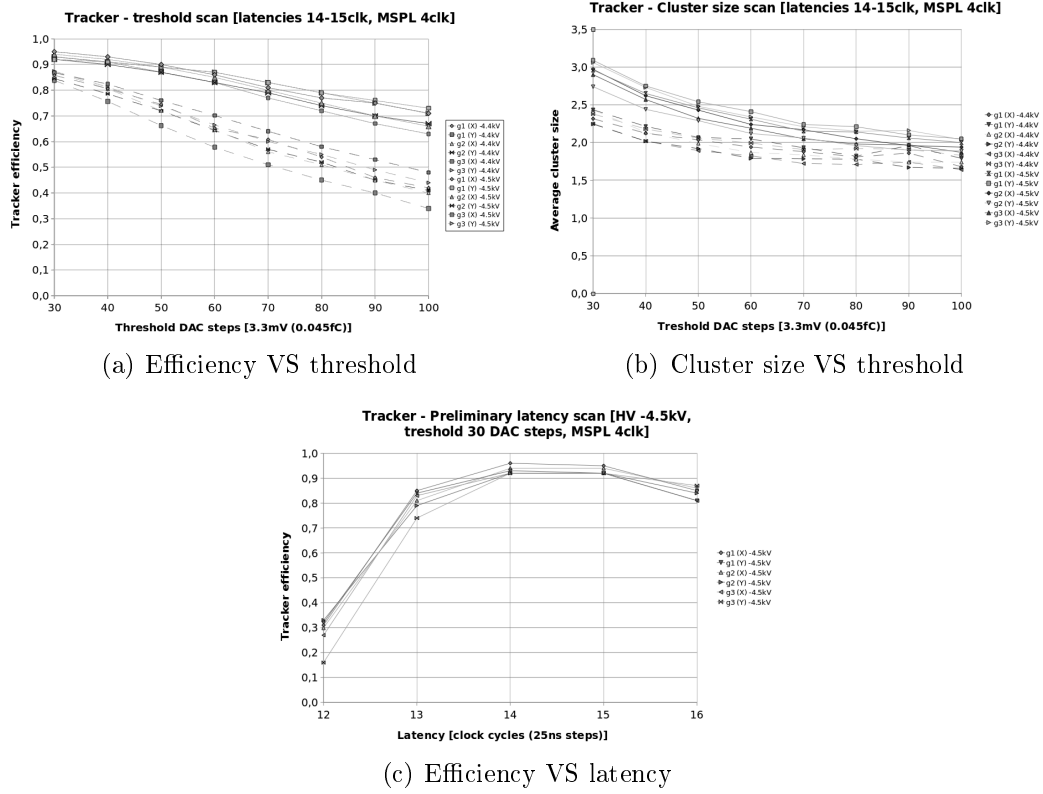


Figure 3.1: Preliminary tracker tests

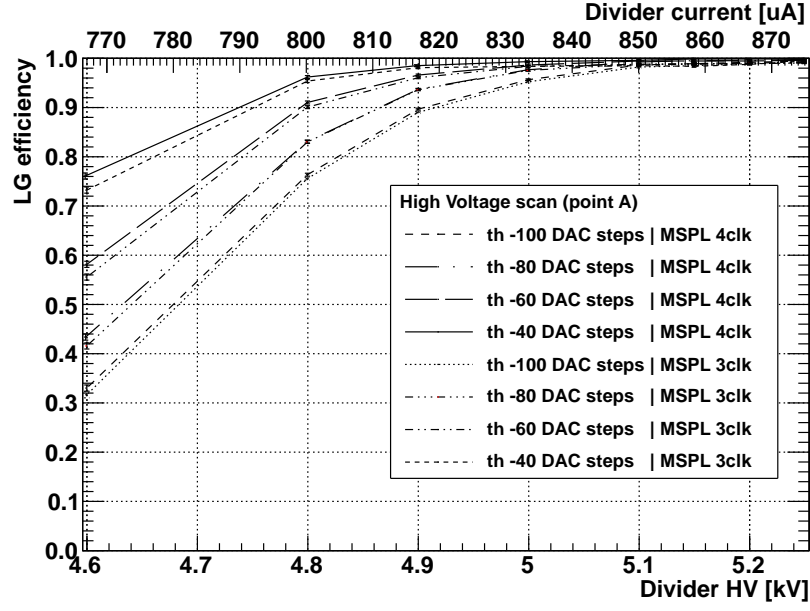
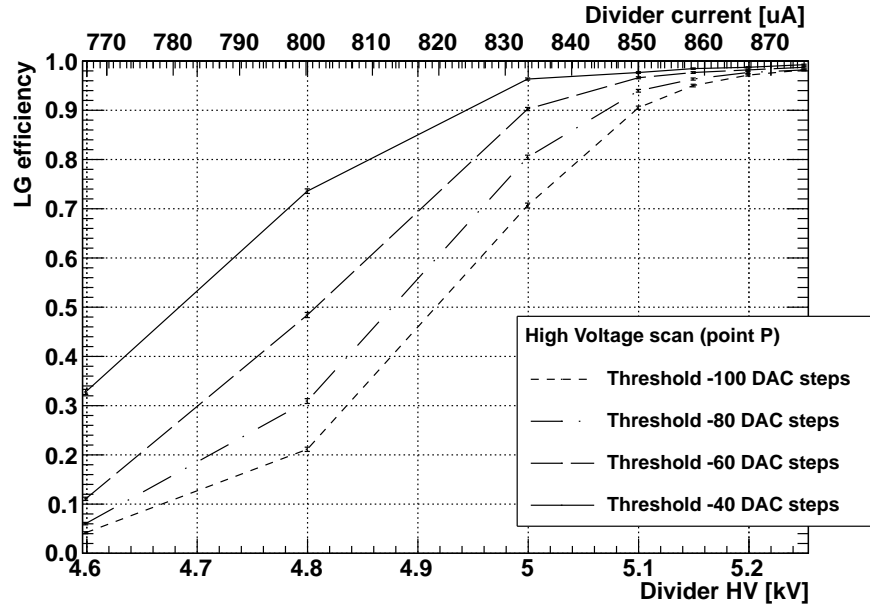
(a) Beam on *zone A* pads(b) Beam on *zone P* padsFigure 3.2: High voltage scans performed with beam on zones *A* and *P*

Figure 3.2(a) on the facing page shows the results of the HV scan performed when the beam was centered on A, while Figure 3.2(b) shows the results for P.

Major efficiency at lower HV values is noticeable on the region made of smaller pads. This effect may be due to the capacitance of the pads themselves, which affects the signal where the pads are large. A study was done about this and will be presented later in this thesis.

In zone *A* we reached an efficiency of about 95% or higher, at thresholds $-40ds$ and $-60ds$, already with a divider current $I_D = 817\mu A$, and at $I_D = 850\mu A$ we got $\varepsilon \simeq 98\%$ for all the four threshold values. $MSPL = 3clk$ graphs do not diverge appreciably from the $MSPL = 4clk$ ones. Instead, in zone *P* the LG prototype approached the full efficiency for all thresholds only at $I_D \geq 866\mu A$, with $\varepsilon > 95\%$ at $I_D = 850\mu A$ only for $th = -40ds$ and $th = -60ds$ data sets.

We also made an HV scan after changing the detector gas mixture, as described in Chapter 3.4 on page 37. We added CF_4 inside the detector, resulting in a lowering of the gain. Figure 3.3 on the following page shows a comparison of the prototype efficiency with its standard gas mixture (Ar/ CO_2 70/30) and with CF_4 (Ar/ CO_2 / CF_4 60/20/20). I will come back on the purpose of this scan in Chapter 3.4 on page 37.

The loss of efficiency at lower current levels may be reduced by optimizing the divider in order to work with CF_4 , changing the internal electric fields of the detector.

3.3 Threshold scan

We performed an efficiency scan as a function of VFAT2s threshold level for two different regions of the chamber (*A* and *P*). This is particularly useful if one wants to understand how much the threshold can be raised (for example,

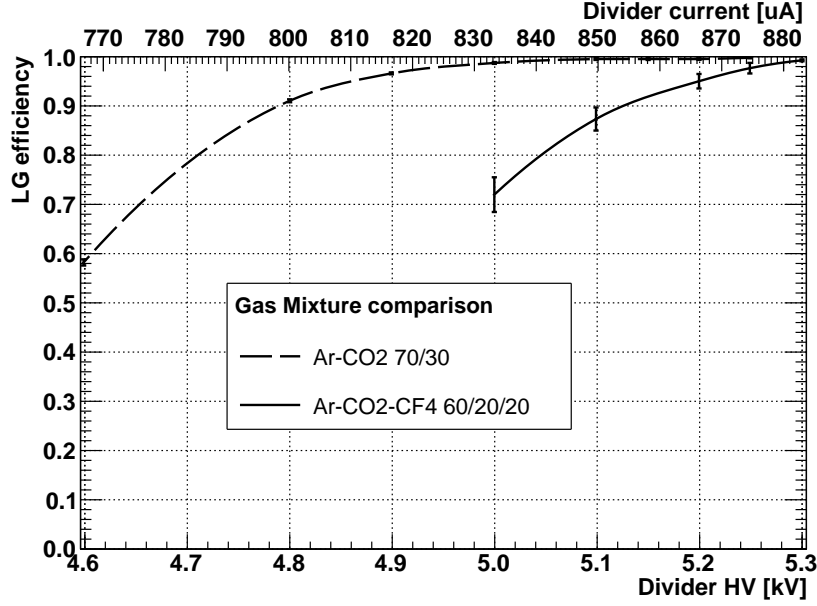


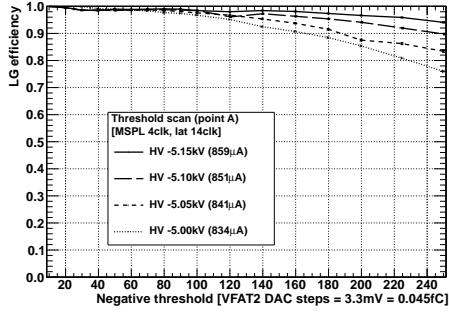
Figure 3.3: High voltage scan performed using an Ar/CO₂/CF₄ 60/20/20 gas mixture (same internal voltages and fields as for Ar/CO₂)

to work in noisy environments) while avoiding an important loss of efficiency. We did not use the *TrimDAC* feature, as we were setting the same threshold for all the channels of all the VFAT chips at a time.

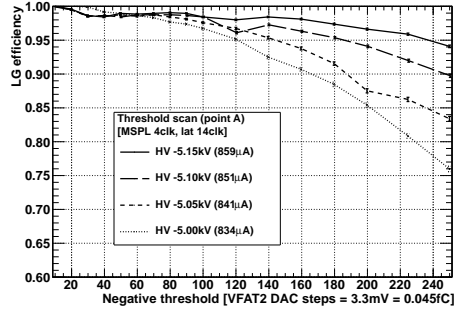
Figure 3.4 on the facing page shows the results of the test. Again, *zone P* looks less efficient than *zone A*; however the response of the chamber is satisfying: when working at high gain (referring to the sets of data taken at divider current $I \geq 850\mu A$) we can arbitrarily raise the threshold to $th = 90ds$ without virtually experiencing any efficiency loss.

The plots in Figure 3.4 also display an ostensible full efficiency ($\varepsilon \simeq 100\%$) at $th < 30ds$. If we compare this result to those seen in Chapter 2.2.1 on page 27, it is clear that we are inside the noise interval: the efficiency seems high, while we are actually detecting more noise hits than particles.

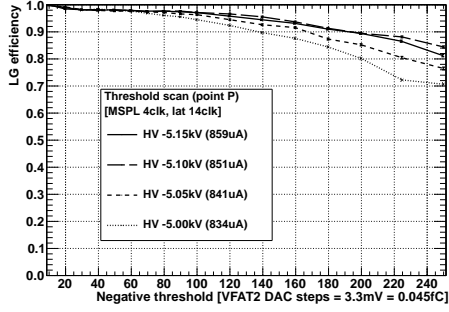
Does our prototype's gain depend on charging up effects? Any prelimi-



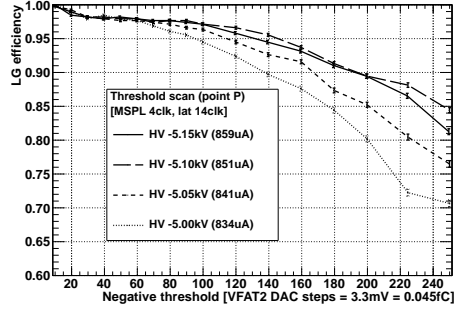
(a) Point A



(b) Point A (zoom)



(c) Point P



(d) Point P (zoom)

Figure 3.4: Threshold scan results for *zone A* and *zone P*

nary extracted gain curve may be inadequate when a detector is be put, for example, in front of the LHC beam line, where the luminosity is way higher than what you can get with an X-Ray gun or during a test beam. One would need a way to repeat the gain measurement once the detector is lying in its final configuration.

We may think to check the gain using efficiency measurements as a function of threshold. In our case, the readout electronics consists of digital chips (*VFAT2*): because of the ADC blocks at the end of each channel, the analog signal is integrated; otherwise the efficiency versus threshold plots would resemble the Landau energy loss distribution (multiplied to the gain of detector) superponed to a Gaussian noise distribution centered in zero.

Assuming that:

1. incoming particles are *MIPs*, so that they lose energy almost only by ionization ($\Delta E \propto Q$);
2. the whole charge released by a MIP is collected by a single electrode¹,

so that $\Delta E_{MIP} \propto Q_{IN} \propto Q_{DETECTED}$, where Q_{IN} is the charge relased in the drift region. One can then simulate (e.g. with *Garfield*) the loss of energy of a MIP and the average ionization potential for the gas mixture in use, therefore tracing the initial charge Q_{IN} . In $3mm$ of Ar/CO₂ 70/30 we have $\overline{Q_{IN}} \simeq 28 \text{ e}^-$.

The energy loss distribution, when few interactions cause the whole ΔE , is given by:

$$f(\lambda) = \frac{1}{\sqrt{2\pi}} e^{-\frac{1}{2}(\lambda + e^{-\lambda})} \quad , \quad \lambda = \frac{\Delta E - \Delta E_{MP}}{K \frac{Z}{A} \frac{\rho}{\beta^2} X}$$

where ΔE_{MP} is the most probable energy loss (the peak of the Landau distribution, see for example Figure 3.5 on page 38) and λ represents the

¹The diffusion of electronic avalanche in $9mm$ of Ar/CO₂ 70/30 is Gaussian and has $\sigma \simeq 300 \div 400 \mu m$.

normalized deviation from ΔE_{MP} [11].

We can now fit the fine efficiency versus threshold histogram we got with the reverse integral of the simulated Landau distribution:

$$F(V_{TH}) = G \cdot \int_{V_{TH}}^{\infty} f(\lambda) d\lambda$$

using G , the gain of the chamber, as a parameter to be found minimizing the χ^2 .

Another interesting parameter of the fit would allow the conversion from *VFAT2 DAC step bins* to charge expressed as number of electrons; it is the number of electrons n_{e^-} which total charge corresponds to the amplitude of each threshold step. For the fit to be coherent we found $550 \leq n_{e^-} \leq 1050$, which is really reasonable: in principle, the minimum ΔQ read by VFAT2 ADCs should be $LSB_{ADC} = 0,8fC = 500 \text{ e}^-$ [5].

Figure 3.6 on the next page shows the results of this study². The Landau integral fit covers just a selection of threshold values: an upper bond is needed since the ADC loses linearity at around $n_{steps}^{MAX} - 10\% \simeq 230ds$, while a lower bond prevents us from messing with the noise Gaussian. The latter was set at $-50ds$, which was found to be enough to cut the noise out.

This was a very preliminary analysis, which may be refined in order to prove the efficiency of this method, aimed at checking the gain of proportional chambers in their final setup.

3.4 Timing scan

We worked on some time-performance scans as well, to check how fast was the prototype reponse, and what could be done to improve the signal timing.

²Study performed by Eraldo Oliveri (University of Siena - INFN Pisa).

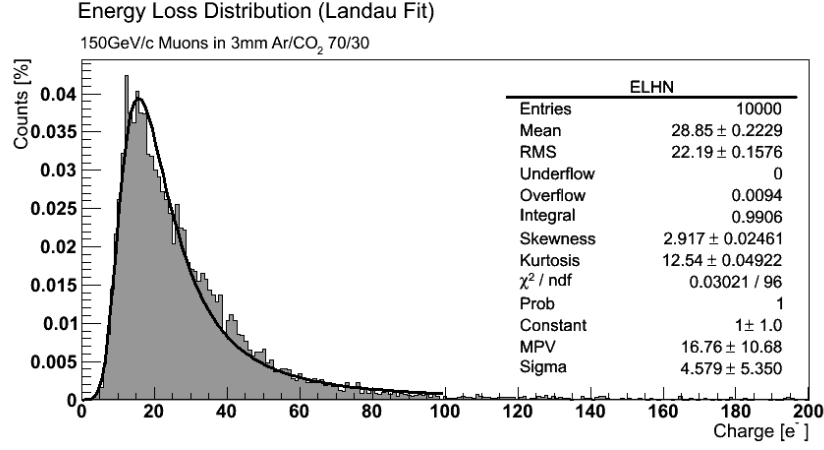


Figure 3.5: Simulation of MIPs energy loss distribution in the detector (*Garfield*)

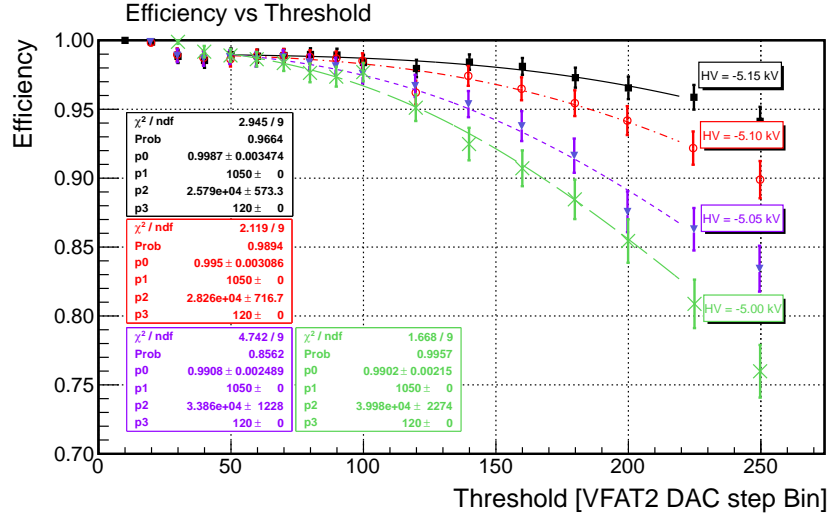


Figure 3.6: Efficiency versus threshold scan fitted by the integral of a Landau energy loss distribution

First we estimated the latency via the LabVIEW software we were using to interact with the VFAT chips, and it appeared to be around 17 *clock cycles*. Then we investigated all the latencies in the $[10clk, 19clk]$ interval with a set of acquisitions at different thresholds and MSP lengths.

Figure 3.7 on the following page shows all the data sets. Efficiency is plotted versus latency; indeed, the signal appears to start at 17*clk*, and the efficiency approaches 90% only at low thresholds or at $MSPL \geq 3clk$. This is due to the threshold-crossing time spread of the detector, when filled with Ar/CO₂, that is longer than a single clock cycle (the average spread is about $\sim 70ns$ while a clock cycle lasts 25*ns*). We can select two efficient working points:

1. $MSPL = 4clk$, with any threshold value such that $40ds < th < 100ds$;
2. $MSPL = 3clk$, with threshold $40ds \leq th \leq 60ds$.

The former was largely used during the whole test beam period, but it compels the detector to work at low time performance, which however was not a problem for these tests. The latter setup provides a faster response, but does not shelter us from catching noise hits (at $th = 40ds$, see below) and we would lose a part of the signal if an higher threshold is set.

We clearly get some noise at $th = -40ds$. The dotted lines show that the detector is acquiring signal even out of the right latency range: that signal is not related to the beam and it is caused by noise. This is confirmed by the increase of the hit counts when the MSPL lenghtens: by setting a longer MSPL we just integrate the signal (both the "real" one and that due to the noise) over a longer time interval.

In Figure 3.8 on page 41 I am explaining this behaviour, showing $MSPL = 2clk$ and $MSPL = 4clk$ data sets. For both, thicker lines represent high thresholds and thinner lines stand for low thresholds. The large GEM's efficiency does not fall to 0 outside the latency boundaries; indeed, where

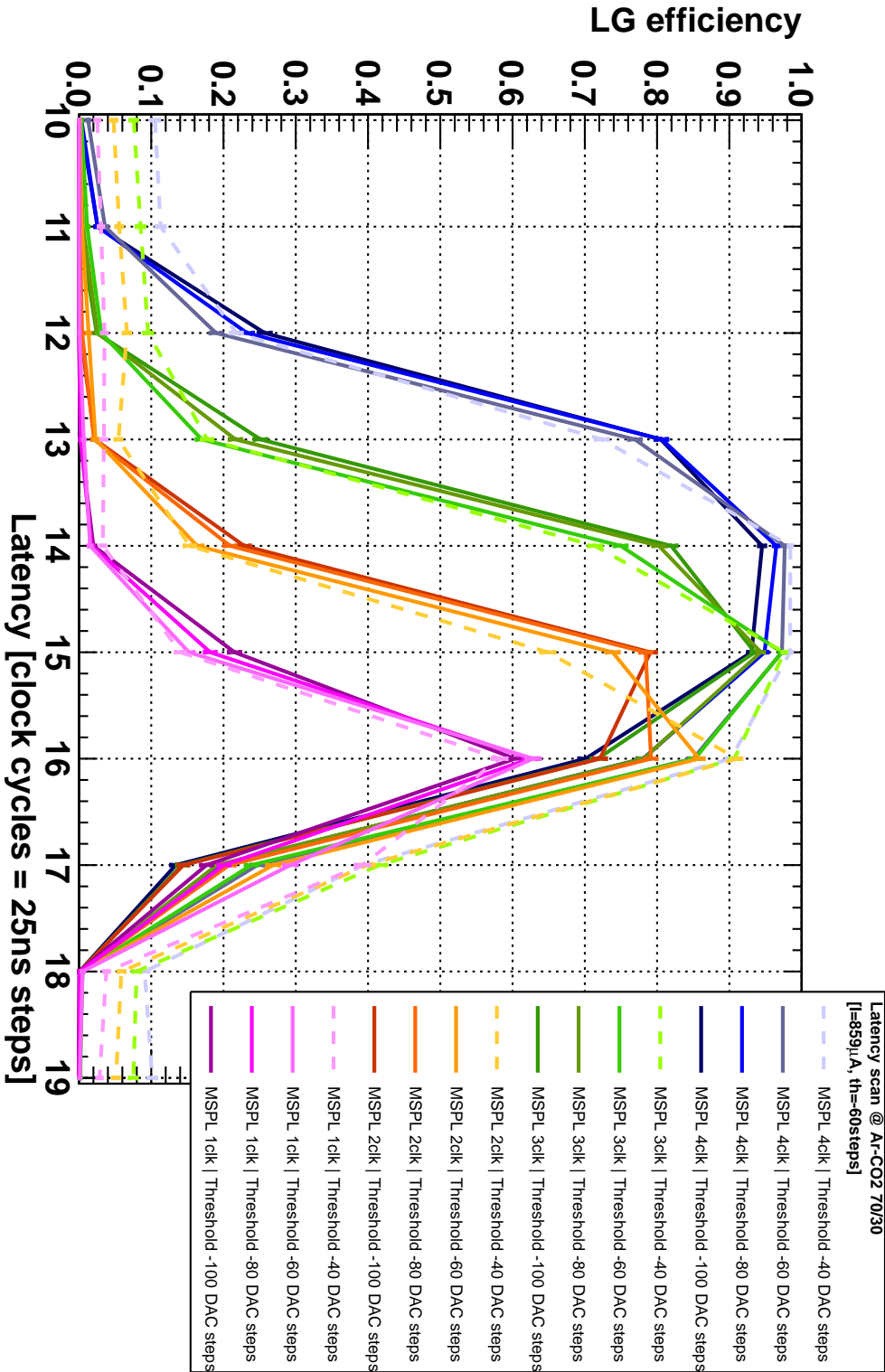


Figure 3.7: Latency scans performed at four different $MSPL$ values. Data sets were taken at various threshold values between $-100ds$ and $-40ds$, during a μ^- beam.

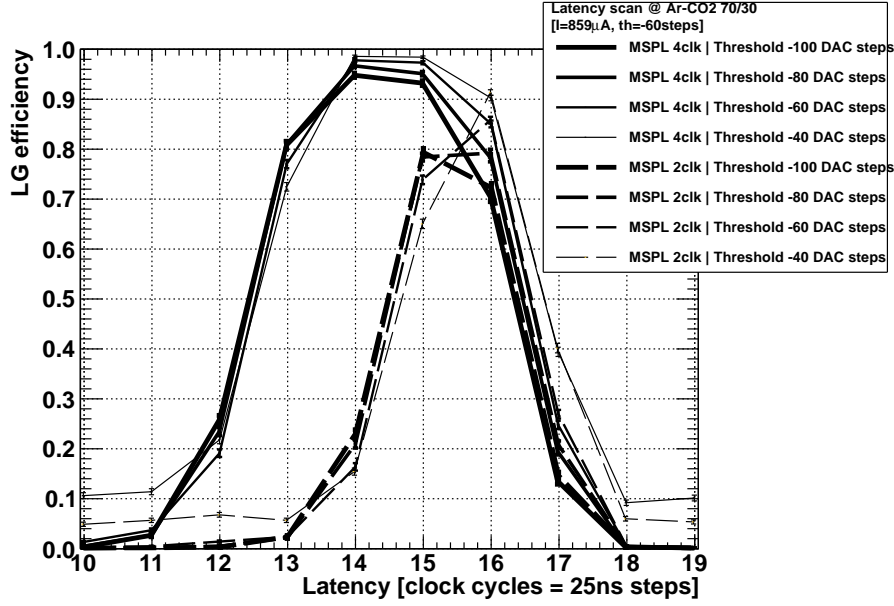


Figure 3.8: Noise counts become visible at $th \leq 40ds$

$th \geq 40ds$ efficiencies are null, we see that:

$$\mathcal{E}_{MSPL=4clk}^{th=40ds} \simeq 2 * \mathcal{E}_{MSPL=2clk}^{th=40ds} \quad (lat \leq 11clk \vee lat \geq 18clk)$$

Noise hits are indeed integrated for double the time.

An histogram of the time intervals between the scintillators trigger and the VFAT2 *Fast-OR* trigger³ provides more data about the time resolution of the whole DAQ system⁴. The more narrow this distribution is, the higher is the time resolution, which indeed is the *RMS* of the plot in Figure 3.9 on the following page.

³Study performed by Eraldo Oliveri (University of Siena) during the previous test beam period (June 2010).

⁴DAQ stands for Data Acquisition. Here the DAQ system is made of a large GEM detector with a pad readout, and VFAT2 front-end chips.

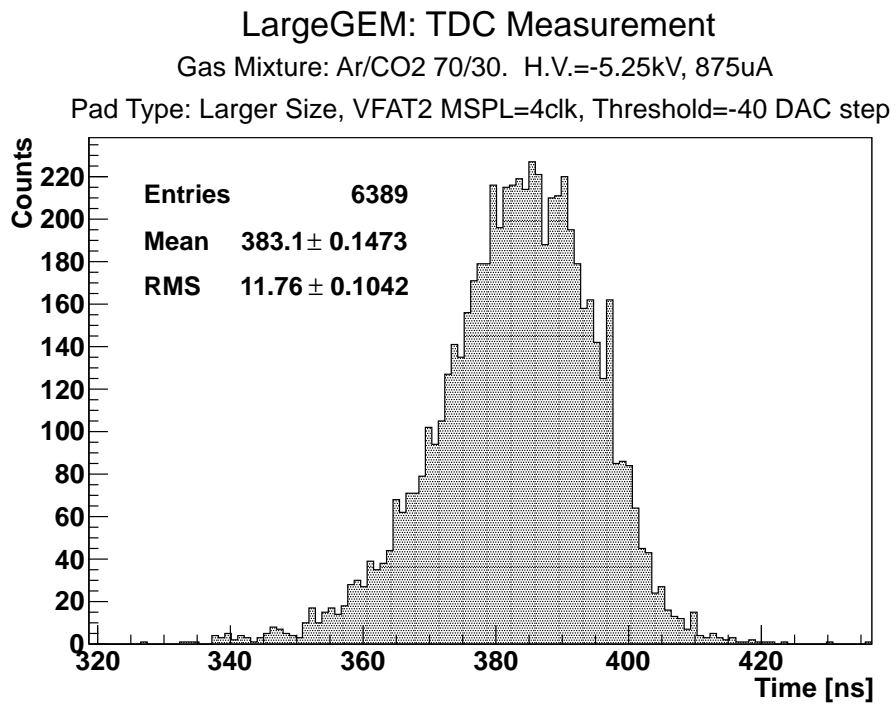


Figure 3.9: Distribution of elapsed time between scintillators and VFAT2's *Fast-OR* trigger signals

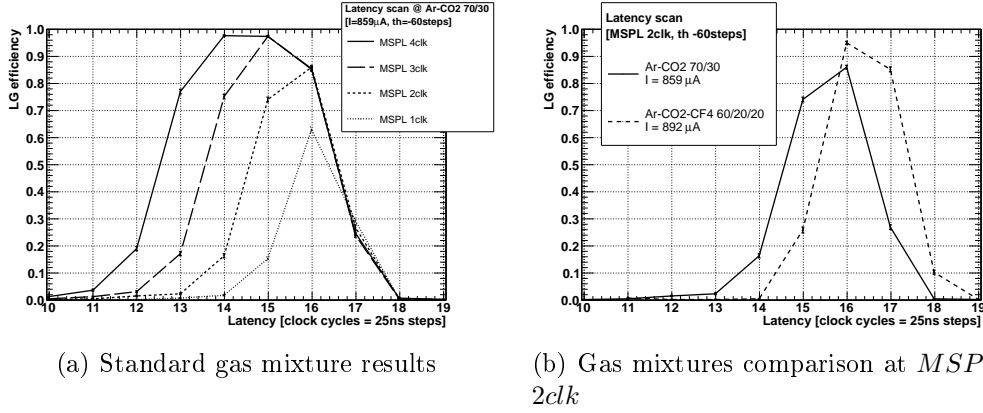


Figure 3.10: Data taken adding CF_4 to the standard Ar/ CO_2 70/30 gas mixture (same internal voltages and fields as for Ar/ CO_2)

The same Figure 3.9 also shows that:

$$\frac{< TDC >}{1clk (25ns)} = \Delta t_{(SC_{trigger} \rightarrow FastOR_{trigger})} \simeq 15clk$$

which is only relevant if we can't set the right latency (it will be $lat \geq \Delta t$).

Increasing detectors time performance is a priority. The LHC should start working at very high frequency and intensity by the end of 2011. The spot where some TOTEM GEM detectors are inserted is very near to an interaction point, and therefore they run through extreme radiation conditions. We made a test trying to find some new setup for those TOTEM detectors, which would allow them to have a faster response without changing the divider setup.

A percentage of CF_4 was added to the gas mixture inside the LG, getting to an Ar/ CO_2 / CF_4 60/20/20 configuration. After the High-Voltage scan described in we repeated some of the latency scans, the results of which are compared to those we got with the previous gas mixture in Figure 3.10. We focused on $MSPL = 2clk$ tests since a length of $2clk$ would be fitting for TOTEM future runs purposes. Figure 3.10(b) clearly shows that if CF_4 improves the response speed of this kind of detectors: the new gas mixture

allows to approach the full efficiency at $th = -60ds$ and $MSPL = 2clk$. On the other hand, we need to supply a little more current, which however might increase the discharge probability in a high-radiation environment; the LG prototype was not damaged by the HV we applied for these tests, but its tolerance is yet to be tested at those levels.

The fact that the detector was designed to work with Ar/CO₂ 70/30 is to be noticed: by optimizing its divider for this new gas mixture we may improve the detector's time resolution without affecting its gain too much.

3.5 Behaviour with hadron beam

The efficiency of this detector proved to be higher when detecting hadrons, as was demonstrated by tests with pion beams (see Figures 3.11 and 3.12).

Figure 3.11 shows that the pions HV scan was performed for different in-

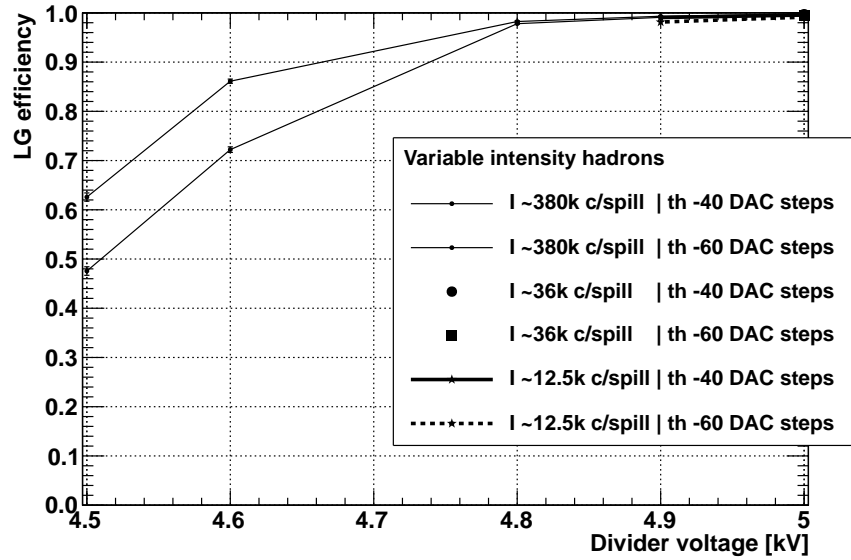


Figure 3.11: High-voltage scan under a beam of pions

tensities of the beam (however, note that for some intensity-threshold combinations we only got few data). Figure 3.12 on the facing page only shows

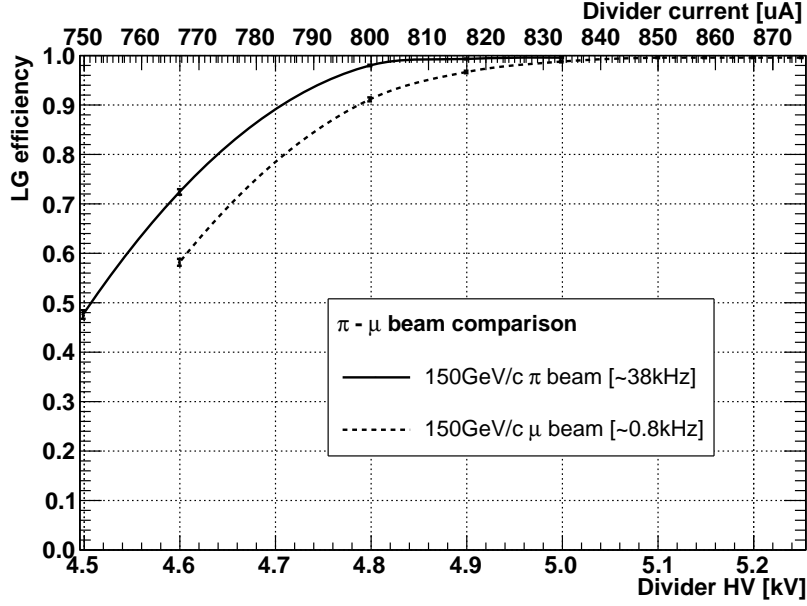


Figure 3.12: Detector behaviour: comparison between pions exposition and muons exposition

the data taken when the beam intensity was equal to 380.000 particles per spill and the threshold was set to -60 *DAC steps*, in order to compare two scans with the same settings.

An effect of *charging up* occurred in this case: the pion beam was much more intense than the muon beam. Therefore some of the ions produced in the avalanche accumulated on the sides of the insulator holes, which are not perfectly straight, and strenghtened the amplification field, raising the GEM foil gain with no need of increasing the external voltage. The high-level visible effect is an apparent raise of efficiency at constant divider HV.

Remarks

4.1 (In)homogeneity of the prototype

4.1.1 Chamber borders, spacer frame and foils junction zone

The availability of such a good tracking system let us highlight some defects of the prototype. When we direct a flux of charged particles over a detector, for some reasons the response may vary spatially. For instance, a pad may be disconnected from the corresponding pin on its VFAT chip; or we may have pointed the beam over a region of the detector containing a piece of the spacer frame.

Figures 4.1 on the next page and 4.2 on page 49 display a radiography of the LG prototype, made by moving the detector around in order to check the response of several areas (see Figure 1.4(b) on page 13). The graphs plot the two-dimensional beam profile as it was detected by the tracker, with the condition that there were hits on the LG in correspondence to those tracks. We spotted:

- *dead* (disconnected) pads: see Figures 4.1(d), 4.1(e) and 4.2(c);
- thin spacers: see Figures 4.1(b), 4.1(h), 4.2(b), 4.2(c), 4.2(d) and 4.2(f).

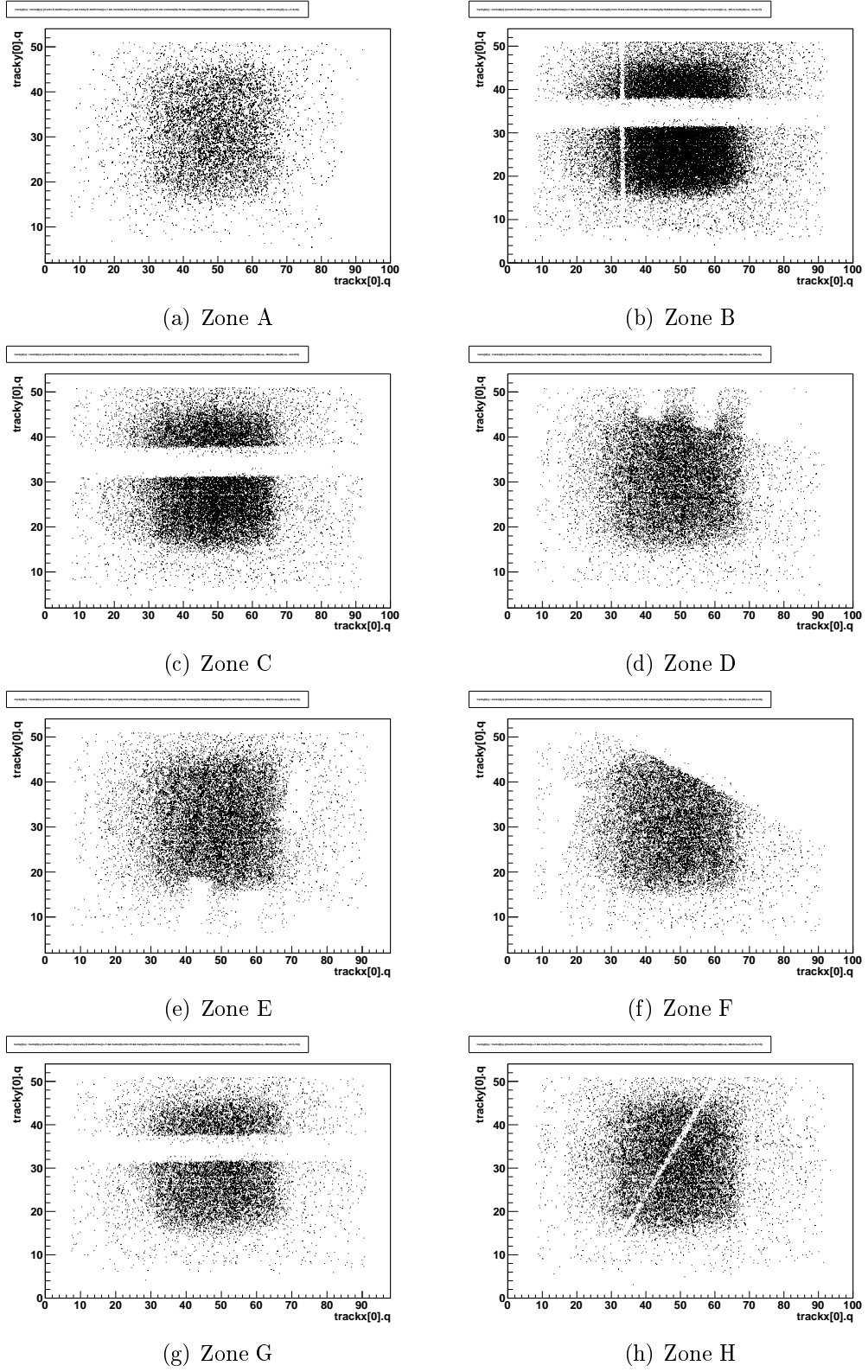


Figure 4.1: A radiography of the prototype triple GEM detector

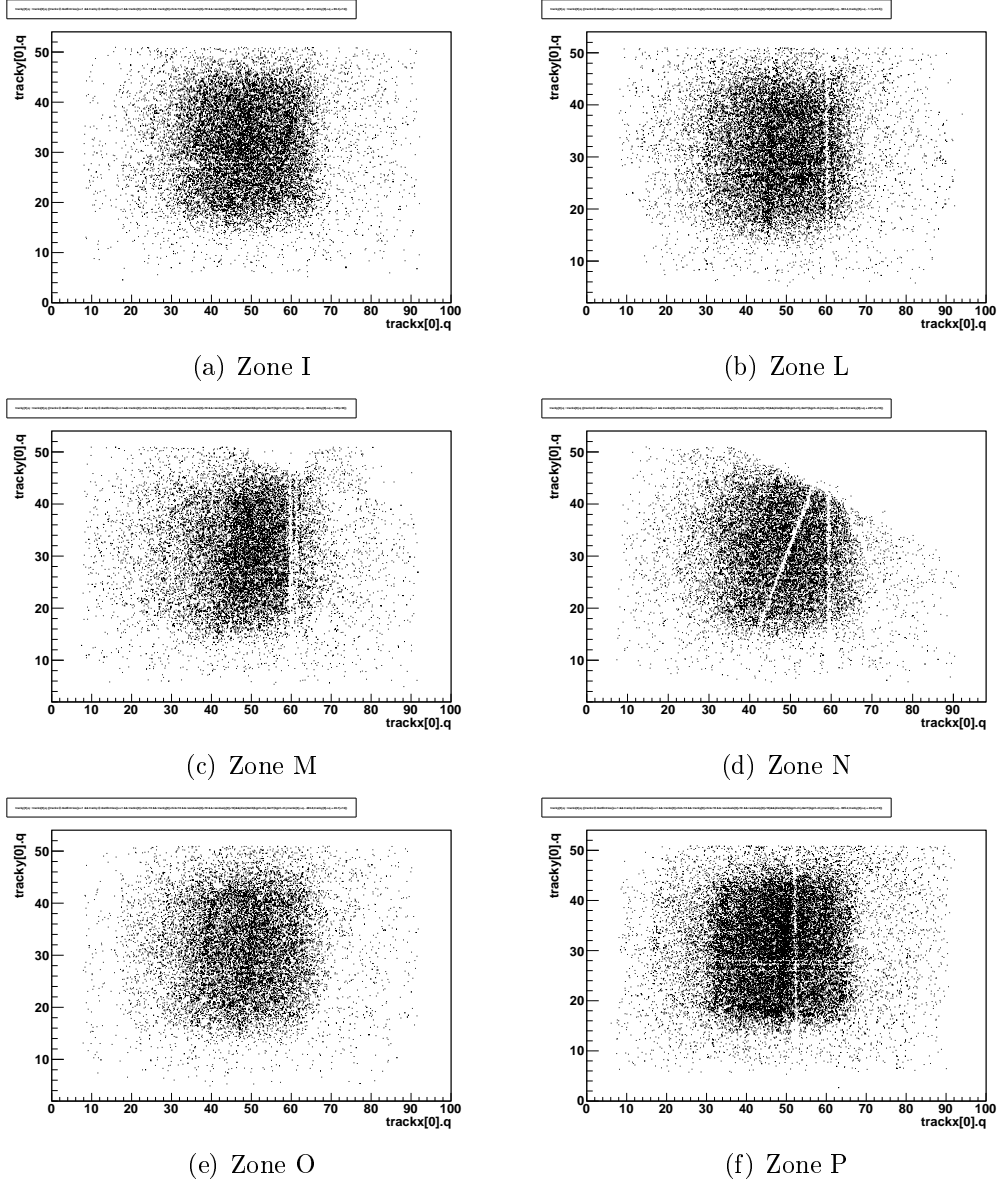


Figure 4.2: A radiography of the prototype triple GEM detector

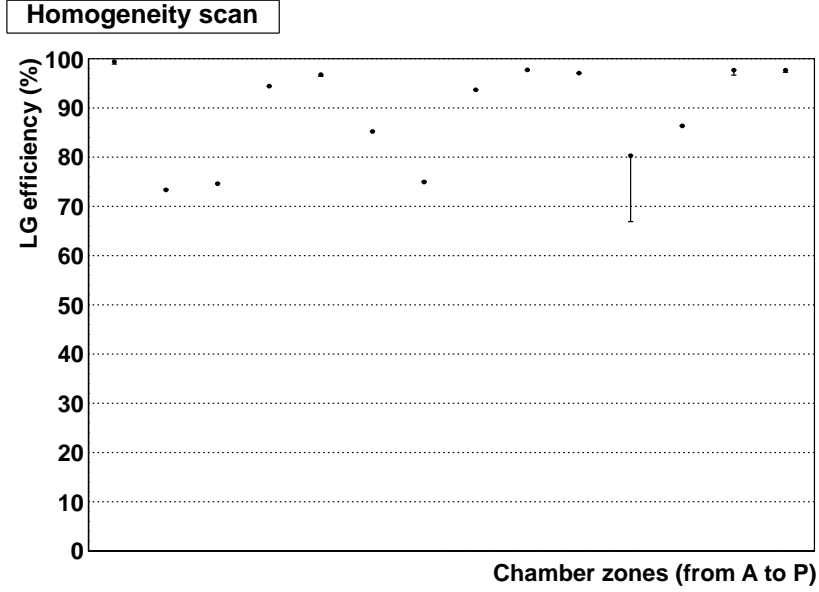


Figure 4.3: Efficiency scan over various critical chamber regions

In particular, Figure 4.2(c) shows a misalignment between a spacer and, probably, the edge of a cathode sector;

- segments of the thick central spacer covering the GEM foils seam: see Figures 4.1(b), 4.1(c) and 4.1(g);
- the edge of the chamber: see Figures 4.1(f) and 4.2(d).

Figure 4.3 and Table 4.1 on page 57 show the computed average efficiency for all these zones, and some more information that will be discussed below.

A deeper study of the response of the detector in the junction area (Figure 4.4 on the facing page) shows the steepness of the slope in the curve of the efficiency as a function of y (which means, moving towards and across the spacer). This means that the low-efficiency area around the spacer is narrow, as one would require. No collateral malfunctionings were observed in spacer, border and junction areas.

However, it also shows a new problem: the side of the detector which

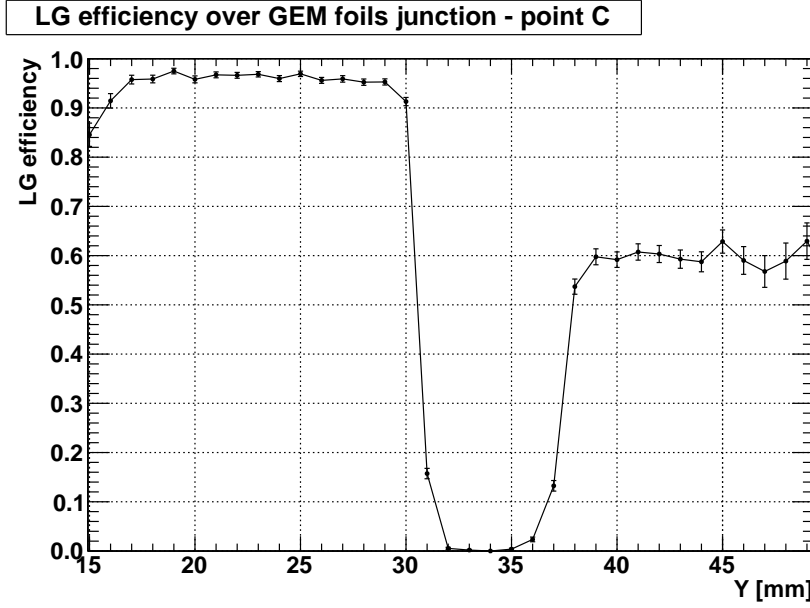


Figure 4.4: Loss of efficiency at the GEM foils junction

wasn't directly involved in the test beam looks less efficient. This effect is too high to be explained in terms of lack of *charging-up*, and it is visible in all the three junction zones we analyzed. It is not either due to visible asymmetries within the voltage distribution boards of the two sides of the chamber: both HV input impedances were measured to be equal to $5,40M\Omega$; it is still possible that the voltage dividers, despite their equal total impedance, are slightly different and provide diverse amplification fields.

We came across this matter after the test beam period was finished and were not able to setup another irradiation test for it. A new gain curve is needed and will be computed as soon as possible with Cu X-Rays, for comparison with the absolute gain calibration made by S. D. Pinto [10].

4.1.2 Effects of the different dimensions of the pads

Larger copper pads should have bigger capacitance. Comparing the two Figures 3.2(a) and 3.2(b) on page 32, one can imagine that the loss of efficiency

in *zone P* is due to the bigger pads capacitance¹, bringing noise and signal coupling.

An off-beam analysis was performed, injecting growing calibration charge pulses to all of the pads via the VFAT2 chips, and fitting the *S-Curves* of each channel with an **erf** function.

The **error function**, also known as **Gaussian error function**, is defined as:

$$\text{erf}(x) = \frac{2}{\sqrt{\pi}} \int_0^x e^{-t^2} dt$$

Once we have defined a threshold for the VFAT chips, and we start injecting charge, as long as the injected potential ($Q = CV$) is under threshold ($\Delta V < th$) the output of the comparator will be low. Then, like an **heaviside step function**, it would go high as soon as the pulse amplitude will overcome the threshold. Actually, it is not so simple: adding the contribution of the noise in the shapes of the calibration pulses (see Figure 4.5 on the facing page), the certainty of rising over threshold at a certain charge value becomes a Gaussian probability, centered around the threshold value.

An **S-Curve** is an histogram of hits whilst varying the injected charge for a given threshold [4]; it corresponds to the shape of the **erf** function. Indeed, one can obtain the same plot if he integrates the Gaussian distribution of the noise for one VFAT channel, given that he knows the width of that distribution. Once that an S-Curve is fitted with an **erf** function, the noise distribution's width is the *sigma* of the **erf**, and the mean value corresponds to the threshold potential².

Figure 4.6(b) on the facing page allows us to state that the lack of effi-

¹The pads at *point P* are the largest that we tested at this time; pad capacitances were measured to be about 60 to 100pF.

²Actually, we fit the S-Curve with an **erf** function. ROOT stores the fit functions as objects, and makes their parameters (mean, RMS, *sigma*, and so on) available via calls to the objects itself. To compute the *sigmas* of Figure 4.6(b) on the next page, we fitted all of the S-Curves with **erf** functions and plotted their *sigma* parameters.

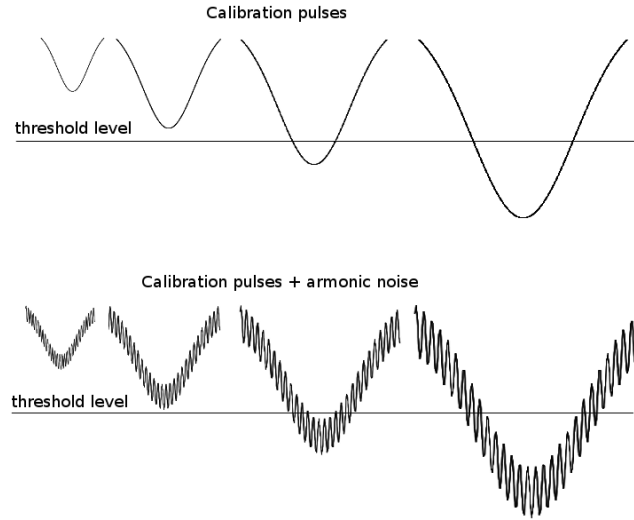


Figure 4.5: How a calibration pulse scan works

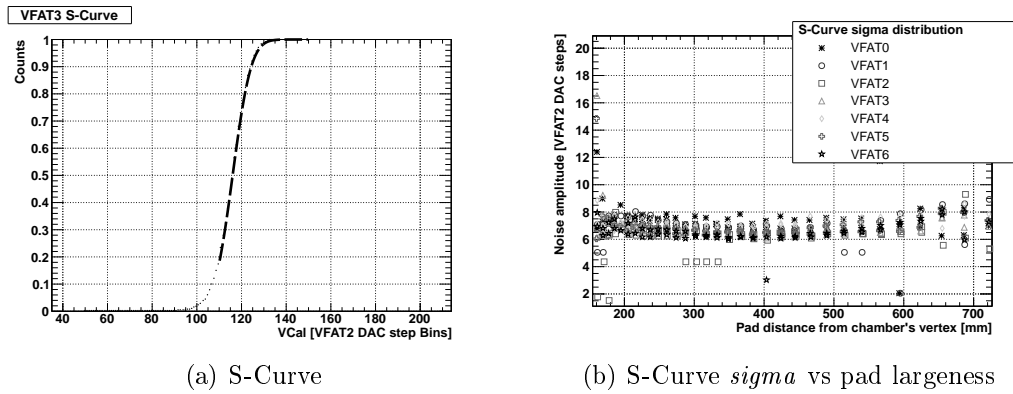


Figure 4.6: An S-Curve fitted by an `erf` function. On the right, the standard deviation (σ) of the pad's S-Curve is plotted as a function of the radial position of the pad in the detector, and thus as a function of its increasing largeness.

ciency of *zone P* pads is not caused by their parasitic capacitance: the bigger pads (those at the right side of the plot) do not show an appreciable increase of the noise. There should be another reason for the difference in response between *point P* and *point A*. We will perform more tests as soon as possible.

The pad-based readout plane appears to work properly, and it could be a proper solution to adopt for large gaseous detectors. A pad readout simplify the data analysis process, since one does not have to provide coincidence within more readout layers (as it is for strip-based systems) to understand where an event has occurred.

4.2 Data analysis system efficiency

4.2.1 Efficiency radius

In Chapter 1.5.1 on page 20 I explained how the efficiency is computed. If an hit occurs in the Large GEM within a fixed radius (an *efficiency radius*) from the projecton of the track of the particle, then we say that the chamber has been efficient. If there is not any hit within the efficiency radius, it has been inefficient.

What happens if we set a wrong efficiency radius? There are two scenarios:

1. the radius is too short. In a large-pads area we may not include a whole pad within the radius, and the efficiency-computing algorithm would act wrong.
2. the radius is too long. Some noise hits on adjacent pads may be mistaken as efficient hits.

The average electron cloud produced in the avalanche has about a $3mm$ diameter, so we are sure to include all of the charge if we set a radius as long as it is enough to cover whole pad of the smallest one. Figure 4.7 on the facing page shows the fluctuation of the computed efficiency, for every zone we checked, for different efficiency radius values. It appears then clear that $ef_{\text{frad}} \geq 20mm$ would be fitting for every scan.

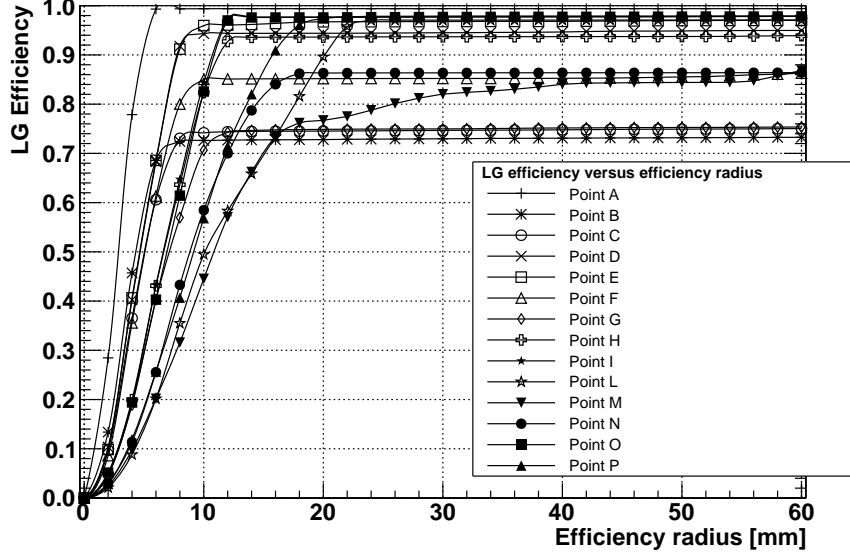


Figure 4.7: Efficiency radius scan: how changing the radius influence the efficiency computing algorithm. Large GEM working point: $HV = -5, 15kV$, $th = -40ds$

Actually, all the result displayed in this text were computed trying to minimize the efficiency radius for each zone of the chamber, just to include the minimum possible amount of noise hits. For each set, the efficiency radius was set equal to the minimum of those for which the efficiency was in the *plateau* of the curve.

The plot of Figure 4.7 is also satisfactory because it shows that the noise level is low for each zone, with the exception of *point M*: the *plateaus* are very flat, which means that enlarging the radius does not mean including many noise hits. *Zone M* was probably adjacent to two noisy channels, one at a distance of about $20mm$ and the other, less noisy, about $35mm$ far, as one can see from the plot.

Playing with the acceptance length may provide more interesting results. For example, if I take a couple *HV scan* data sets from Figure 3.2(a) on page 32 and arbitrarily set wrong *offsets* (see the following section for a deeper

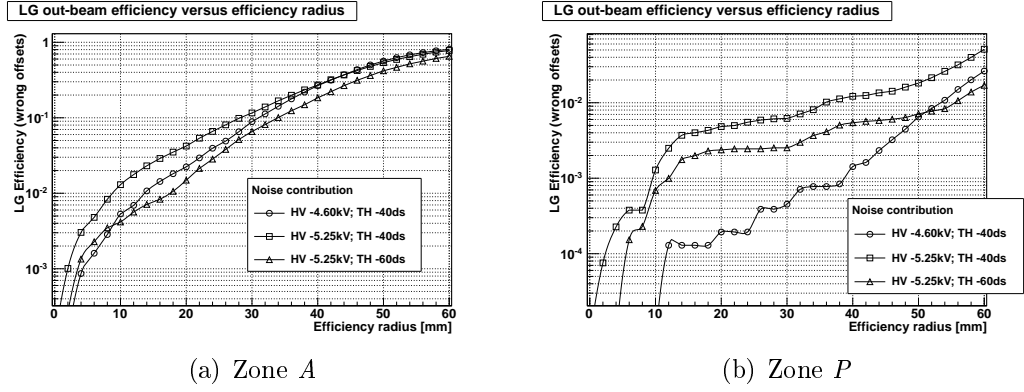


Figure 4.8: Off-beam efficiency computation: evaluating the contribution of noise

explanation), going to look for hits in a part of the chamber which was not beam irradiated, an efficiency radius scan will show me the contribution of pure noise to what we call the detector's efficiency. Stretching the radius, I indeed allow the software to look for hit channels in a larger region of the chamber, therefore including more noise. Table 4.1 on the next page shows, for each scanned zone:

- the best efficiency radius, according to Figure 4.7;
- the level of efficiency of that chamber sector, computed with the stated “best radius” (see Figure 4.8³), while the sector was not under beam.

The errors in the efficiency column are statistically computed. They have to be added to those of the following column.

Table 4.1 gives of course a precise idea of how the noise contributes to the computation of efficiency. If we repeat this scan on-beam, these effects would result negligible, because the charge released by incoming particles would dominate.

³Figure 4.8(a) shows that *zone A* lies nearby some noisy channels, indeed with an acceptance radius of 60mm the efficiency grows to significant values; anyway, setting $ef_{\text{rad}} = 6\text{mm}$ I prevented the noise to be included in our scans.

Zone	Best <i>effrad</i>	Efficiency	Contribution of noise
A	6mm	$(99,40 \pm 0)\%$	0,5%
B	7mm	$(73,35 \pm 0,11)\%$	0,01%
C	8,5mm	$(74,60 \pm 0,11)\%$	0,01%
D	9mm	$(94,43 \pm 0,03)\%$	0,07%
E	9mm	$(96,76 \pm 0,02)\%$	0,35%
F	9mm	$(85,21 \pm 0,10)\%$	0,03%
G	12mm	$(74,95 \pm 0,14)\%$	0,02%
H	12mm	$(93,68 \pm 0,04)\%$	0,02%
I	12mm	$(97,73 \pm 0,02)\%$	0,13%
L	23,5mm	$(97,07 \pm 0,02)\%$	0,04%
M	30mm	$(80,28 \pm 0,12)\%$	13,38%
N	18mm	$(86,35 \pm 0,09)\%$	0,05%
O	12mm	$(97,67 \pm 0,02)\%$	1,01%
P	18mm	$(97,66 \pm 0,03)\%$	0,43%

Table 4.1: Contribution of noise to the computation of LG efficiency. Efficiency was detected at: $HV = -5,15kV$, $th = -60ds$, $MSPL = 4clk$

4.2.2 Cuts

Chapter 1.5.1 on page 20 points out that tracks are reconstructed only in some simple cases. In addition, during the analysis process some more conditions were requested for the track to be used. It was asked that:

1. there is exactly one *x-track* and one *y-track* per event;
2. $\chi^2 < 10$ for both the *x-track* and the *y-track*;
3. the distance between the hits on the tracker chambers and their first order polynomial fit defining the track is $< 10mm$ for every hit.

Inside a ROOT framework, this corresponds to declaring a `TCut` object to be used as mandatory option while selecting the data to process:

```
TCut goodtr("goodtr","trackx@.GetEntries()==1 && tracky@.GetEntries()==1 && trackx[0].
chi2<10 && tracky[0].chi2<10 && residualx[0]<10 && residualy[0]<10")
```

Most of the analysis processes ran through ROOT's `Draw()` command, that accepts `TCut` objects as options. For the previously seen data sets, to acquire which we had to move the chamber 14 times, we needed to declare each time the position of the chamber in respect to the center of the beam. This was done via `TCut` objects, at the same time as setting the efficiency radius. The following declarations were used:

```
TCut Aeff("Aeff","dist(GetX(bgch.ch),GetY(bgch.ch),trackx[0]->q - 240.8,tracky[0]->q +
6.3)<6")
TCut Beff("Beff","dist(GetX(bgch.ch),GetY(bgch.ch),trackx[0]->q - 303.2,tracky[0]->q -
34.4)<7")
TCut Ceff("Ceff","dist(GetX(bgch.ch),GetY(bgch.ch),trackx[0]->q - 362.9,tracky[0]->q -
34)<8.5")
TCut Deff("Deff","dist(GetX(bgch.ch),GetY(bgch.ch),trackx[0]->q - 362.9,tracky[0]->q +
5.6)<9")
TCut Eeff("Eeff","dist(GetX(bgch.ch),GetY(bgch.ch),trackx[0]->q - 362.7,tracky[0]->q +
46.9)<9")
TCut Feff("Feff","dist(GetX(bgch.ch),GetY(bgch.ch),trackx[0]->q - 362.8,tracky[0]->q +
86.2)<9")
TCut Geff("Geff","dist(GetX(bgch.ch),GetY(bgch.ch),trackx[0]->q - 482.6,tracky[0]->q -
34.1)<12")
TCut Heff("Heff","dist(GetX(bgch.ch),GetY(bgch.ch),trackx[0]->q - 482.6,tracky[0]->q +
6.7)<12")
TCut Ieff("Ieff","dist(GetX(bgch.ch),GetY(bgch.ch),trackx[0]->q - 482.7,tracky[0]->q +
86.3)<12")
TCut Leff("Leff","dist(GetX(bgch.ch),GetY(bgch.ch),trackx[0]->q - 663.4,tracky[0]->q -
1.1)<23.5")
TCut Meff("Meff","dist(GetX(bgch.ch),GetY(bgch.ch),trackx[0]->q - 664.9,tracky[0]->q +
108)<30")
```

```
TCut Neff("Neff","dist(GetX(bgch.ch),GetY(bgch.ch),trackx[0]->q - 662.5,tracky[0]->q +
207.3)<18")
TCut Oeff("Oeff","dist(GetX(bgch.ch),GetY(bgch.ch),trackx[0]->q - 483.8,tracky[0]->q +
46.7)<12")
TCut Peff("Peff","dist(GetX(bgch.ch),GetY(bgch.ch),trackx[0]->q - 695.2,tracky[0]->q +
49.3)<18")
```

where the first two numbers in each string represent the position of the chamber for that data set, and the last one is the best fitting efficiency radius.

This approach worked fine. The software did not run across any problem when the variables were declared this way, and the many cuts did not affect the analysis process, since the amount of data taken during the test-beam period was huge.

Conclusions

5.1 Quality of the large GEM prototype

The performances of the detector are within the expectations. No problems were encountered during the on-beam runs: the prototype resisted and detected both lepton and pion beams of various intensities.

As expected, the use of CF_4 improves the time response of the detector, even if the fields and internal structure¹ of the detector are left unchanged. A redesigning of the detector itself and of its high voltage divider will be needed to optimize the performance, and it may be performed together with the LHCb experiment and the group of A. Sharma, whose recent studies were directed in the same direction as ours.

Although the prototype detector worked well, the difficulties encountered during the assembly (most of all, the stretching of large foils, for which there are currently no proper machines) do not justify the advantage of splicing GEM foils together in order to cover larger areas and thus to reduce the number of detectors (S. D. Pinto).

As we will discuss in Chapter 5.2, we needed to test if the detector could

¹the height of the gaps between the GEM foils overall.

work efficiently with the TOTEM readout system. The major problem was the very initial noise due to the coupling of VFAT2 channels with such large capacitance readout electrodes²; it was anyway solved improving the chip grounding on the readout plane.

As a final remark it should be mentioned that these deep investigations were made possible thanks to the RD51-GDD tracker telescope, which could largely improve the resolution and comprehension of the data collected.

5.2 Large GEM detectors in TOTEM and CMS experiments

An aim of August 2010 test beam was to check if a large GEM detector, with a pad based readout, could work well with TOTEM's readout electronics, overall with the VFAT chips.

At the beginning, using those chips with this readout plane seemed impossible, since the noise level was such that virtually no threshold setting could solve any problem. Anyway, after a ground plane was added under the chips, most of the noise was removed. Additional VFAT features, such as *Trim-DAC*, may be used in order to improve the global *SNR* ratio.

RD51 conceived the “*Large GEM*” as a replacement for the current **T1** forward telescope of the TOTEM experiment, at the LHC, which is now made of Cathode Strip Chamber detectors. T1 consists of two arms, each precisely fitting in a gap around the beam pipe and inside the inner surface of CMS, in symmetric positions around *Interaction Point 5*. It covers the pseudorapidity³ region $3, 1 \leq |\eta| \leq 4, 7$.

²60 to 100pF.

³The **pseudorapidity** is defined, starting from the angle θ between the momentum \vec{p} of the incoming particle and the beam direction, as $\eta = -\ln\left(\tan\frac{\theta}{2}\right)$. Therefore, as the angle decreases, $\eta \rightarrow \infty$.

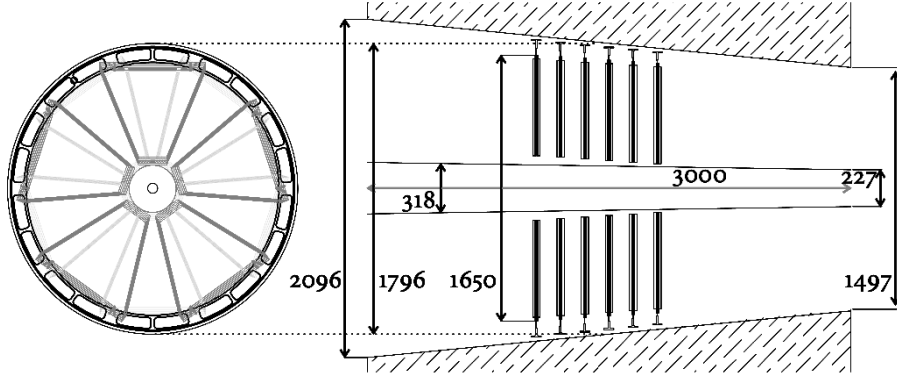


Figure 5.1: An arrangement to replace the current **T1** CSC telescope of TOTEM [9]

A renovation is needed for T1, as its CSC chambers may start suffering ageing effects when the LHC machine will start to run at luminosity $\mathcal{L} \geq 10^{31} \frac{1}{\text{cm}^2 \cdot \text{s}}$. In particular, if that luminosity is overcome by two orders of magnitude, the CSCs would age in few months [7].

The same structure can be built with LG-like chambers, arranging six discs for each arm, where a disc is made of two planes of 5 chambers in back-to-back arrangement (Figure 5.1). Overlap regions would ensure a 360° coverage and allow to adjust the radius of the six discs on demand [10].

As an alternative [7], each disc may be made of six detectors, and they could be alternated in back to back configuration, each disc staggered by $\frac{1}{12}$ from the adjacent ones, to allow overlay. Four such sets would be enough to complete an arm of the future T1.

As in Figure 5.2 on the following page, readout boards would be pad based, like the prototype, featuring $16 \cdot 64 = 1024$ pads of various dimension.

With respect to CSC, GEM chambers offer high rate tolerance, limited discharge probability (less than 10^{-12} at gain $G \simeq 10^4$), high time resolution: for the prototype being analyzed in this thesis, $RMS \simeq 11,8 \text{ ns}$ (see Fig-

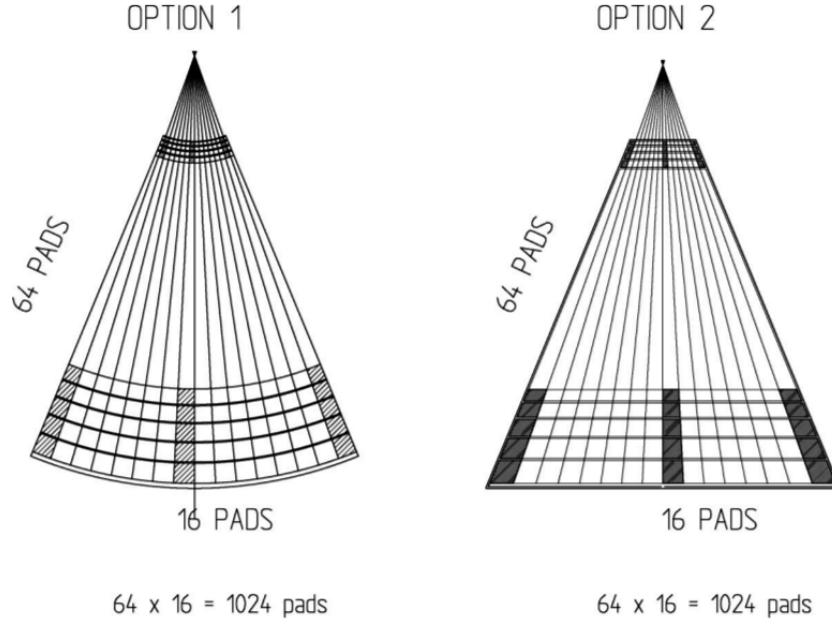


Figure 5.2: Two readout board options for a large triple GEM detector

ure 3.9 on page 42), and it may be improved by adding CF_4 . In conclusion, T1 had been designed for bunch crossing $f \geq 75\text{ns}$ and luminosity $\mathcal{L} \leq 10^{31}$, while a GEM based substitute could in principle survive for years at $\mathcal{L} = 10^{33}$ and would be adequate for faster bunch crossing by just adding a percentage of CF_4 to the internal gases [7].

CMS experiment is also developing similar large GEM prototypes, with a compatible readout, foreseeing a project for muon detecting in the forward region. 50cm wide GEM foils are being produced with no need for splicing.

At the same time, INFN section of Bari is working on LASER ablation of GEM foils, a technique that could ease the automation of mass-manufacturing and possibly increase hole precision and density.

A new branch of GEM detectors has definitely been started.

Appendices

Appendix A

ROOT analysis routines

Two young researchers¹ from **RD51** built the low-level macros used to convert the binary output of the detectors to much more physicist-friendly ROOT *n-tuples*.

My work only consisted of writing down some routines in order to extract efficiency values from specific runs' *n-tuples*, and make the data accessible via plots. The code I wrote is displayed in the following pages.

Listing A.1: *Builder.C*

```
#include <string>
#include <iostream>
#include <TTree.h>
#include <TFile.h>

int EventBuilderVFAT(const char* rawfilename,
                    const char* rootfilename,
                    const int readmaxevent);

using namespace std;

void Builder(string rawfile_address){

    size_t spos;
    size_t substring_lenght;
    string slash = "/";
    spos = rawfile_address.rfind(slash);
    substring_lenght = 7;

    // Extracts the string "Run###" from the rawfile name
    string rawfile_name = rawfile_address.substr(spos+5,substring_lenght);
    // Sets the output file name
    string rootfile_address = "../RootData/" + rawfile_name + ".root";
```

¹Matteo Alfonsi (CERN) and Gabriele Croci (PhD student at University of Siena)

```

// Builds a .root file from a rawfile
EventBuilderVFAT(rawfile_address.c_str(),rootfile_address.c_str(),100000000);
// Sets the reco file name
string recofile_address = "../RootData/" + rawfile_name + "_reco.root";
// Creates a reco file using Offset_Settings.txt
TFile file0(rootfile_address.c_str());
TTree* t = dynamic_cast<TTree*>(file0.Get("rd51tb"));
t->Process("Reco2d_ps.C",recofile_address.c_str());
}

```

Listing A.2: *effex2.C*

```

#include "TFile.h"
#include "TTree.h"
#include "TH1.h"
#include <iostream>

using std::cout;

double effex2(TFile& file0){

    TH1F* heffbgch = dynamic_cast<TH1F*>(file0.Get("heffbgch"));
    double efficiency;
    efficiency = 1 - heffbgch->GetBinContent(1) / heffbgch->GetEntries();
    return efficiency;
}

```

Listing A.3: *efficiency.cc*

```

#include <string>
#include <iostream>
#include <sstream>
#include <TTree.h>
#include <TFile.h>
#include <cstdio>
#include "TVectorT.h"

using namespace std;

double effex2(TFile& file0);

TVectorD efficiency(long int run_number, long int last_run){

    Int_t size = last_run - run_number;
    TVectorD nRun (size+1);
    TVectorD run_eff (size+1);
    Int_t count = 0;

    for (long int i=run_number;i<last_run+1;i++)
    {
        string s;
        char run_n[30];

        sprintf(run_n,"%ld",i);
        s = string(run_n);

        string rootfile_name;
        string recofile_name;

        if (i < 10)
        {
            rootfile_name = "../RootData/Run000" + s + ".root";

```

```

        recofile_name = "../RootData/Run000" + s + "_reco.root";
    }
    else
    {
        if (i < 100)
        {
            rootfile_name = "../RootData/Run00" + s + ".root";
            recofile_name = "../RootData/Run00" + s + "_reco.root";
        }
        else
        {
            rootfile_name = "../RootData/Run0" + s + ".root";
            recofile_name = "../RootData/Run0" + s + "_reco.root";
        }
    }

    TFile file0(recofile_name.c_str());
    double eff = effex2(file0);
    run_eff[count] = eff;
    nRun[count] = i;
    count++;

}

return run_eff;
}

```

Listing A.4: *EffRadius.C*

```

#include <stdlib.h>
#include <string>
#include "TVectorT.h"
#include <iostream>
#include <sstream>
#include <TTree.h>
#include <TFile.h>
#include <TH1F.h>
#include <TGraph.h>
#include <TAxis.h>
#include <TCut.h>
#include <stdio.h>
#include <cstdlib>
#include "TotemMap.hpp"

using namespace std;

TVectorD EffRadius(long int run_number, double xoffsetmm, double yoffsetmm, long int
    minrad, Int_t nsteps){
    TVectorD rad_eff (nsteps+1);
    string run; //Run number to be converted to string
    char run_n[30];
    string offsetx; //Offsets to be converted to strings
    string offsety;

    sprintf(run_n,"%ld",run_number); //Converting run number to a string
    run = string(run_n);
    { //Converting x offset to string
        ostringstream xx;
        xx << xoffsetmm;
        offsetx = xx.str();
    }
    { //Converting y offset to string
        ostringstream yy;
        yy << yoffsetmm;
        offsety = yy.str();
    }
}

```

```

/*
End converting numbers to strings *****
*/

string rootfile_name;
string recofile_name;

if (run_number < 10)
{
    rootfile_name = "../RootData/Run000" + run + ".root";
    recofile_name = "../RootData/Run000" + run + "_reco.root";
}
else
{
    if (run_number < 100)
    {
        rootfile_name = "../RootData/Run00" + run + ".root";
        recofile_name = "../RootData/Run00" + run + "_reco.root";
    }
    else
    {
        rootfile_name = "../RootData/Run0" + run + ".root";
        recofile_name = "../RootData/Run0" + run + "_reco.root";
    }
}

TFile file0 (rootfile_name.c_str());
TTree* t = dynamic_cast<TTree*>(file0.Get("rd51tb"));
t->AddFriend("recotree",recofile_name.c_str());

//Selecting high quality tracks and events
TCut goodtr("goodtr","trackx@.GetEntries()==1 && tracky@.GetEntries()==1 &&
trackx[0].chi2<10 && tracky[0].chi2<10 && residualx[0]<10 && residually[0]<10");
Int_t count = 0;

//Scans radius from mirad to mazrad every 5 millimeters
for (long int i = minrad; i < 2*nsteps + 1; i = i + 2)
{
    string irad; //Converts current radius to string
    ostringstream rad;
    rad << i;
    irad = rad.str();

    string draw_string = "Sum$((dist(GetX(bgch.ch),GetY(bgch.ch),(trackx[0]->q
- trackx[0]->m*400" + offsetx + "),(tracky[0]->q -tracky[0]->m*400" + " + offsety +
")))<" + irad + ") >>h(5,0,5)";

    t->Draw(draw_string.c_str(),goodtr);

    TH1F *h = (TH1F*)gDirectory->Get("h");

    Double_t ieff = 1. - h->GetBinContent(1)/h->GetEntries();

    rad_eff[count] = ieff;
    count++;
}

return rad_eff;
}

```

Listing A.5: *nevents.cc*

```

#include <string>
#include <iostream>

```

```

#include <sstream>
#include <TTree.h>
#include <TFile.h>
#include <TH1.h>
#include <cstdio>
#include "TVectorT.h"

using namespace std;

TVectorD nevents(long int run_number, long int last_run){

    Int_t size = last_run - run_number;
    TVectorD n_events (size+1);
    Int_t count = 0;

    for (long int i=run_number;i<last_run+1;i++)
    {
        string s;
        char run_n[30];

        sprintf(run_n,"%ld",i);
        s = string(run_n);

        string rootfile_name;
        string recofile_name;

        if (i < 10)
        {
            rootfile_name = "../RootData/Run000" + s + ".root";
            recofile_name = "../RootData/Run000" + s + "_reco.root";
        }
        else
        {
            if (i < 100)
            {
                rootfile_name = "../RootData/Run00" + s + ".root";
                recofile_name = "../RootData/Run00" + s + "_reco.root";
            }
            else
            {
                rootfile_name = "../RootData/Run0" + s + ".root";
                recofile_name = "../RootData/Run0" + s + "_reco.root";
            }
        }

        TFile file0(recofile_name.c_str());

        TH1F* heffbgch = dynamic_cast<TH1F*>(file0.Get("heffbgch"));
        n_events[count] = heffbgch->GetEntries();
        count++;

    }

    return n_events;
}

```

Listing A.6: *Recoizer.C*

```

#include <string>
#include <iostream>
#include <TTree.h>
#include <TFile.h>

using namespace std;

void Recoizer(string rootfile_name){

```

```
string run_number = rootfile_name.substr(15,4);

// Sets the reco file name
string recofile_name = "../RootData/Run" + run_number + "_reco.root";

// Creates a reco file using Offset_Settings.txt
TFile file0(rootfile_name.c_str());
TTree* t = dynamic_cast<TTree*>(file0.Get("rd51tb"));
t->Process("Reco2d_ps.C+", recofile_name.c_str());
}
```


Bibliography

- [1] Review of particle physics, 2008. Particle Data Group.
- [2] TOTEM technical design report, January 2008. CERN-LHCC-2004-002.
- [3] The TOTEM experiment at the CERN large hadron collider. In A. Bre-skin and R. Voss, editors, *The CERN Large Hadron Collider: Accelera-tor and Experiments*. CERN, 2009. 2008 JINST 3 S08007.
- [4] P. Aspell. *VFAT2 - Operating Manual*, October 2008.
- [5] P. Aspell. VFAT. In *CMS high- η MPGD workshop*, September 2010.
- [6] R. Bouclier, M. Capeáns, W. Dominik, M. Hoch, J. C. Labbé, G. Million, L. Ropelewski, F. Sauli, and A. Sharma. The gas electron multiplier (GEM).
- [7] S. Lami. Preliminary study for a possible t1 upgrade with large GEMs. In *CMS high- η MPGD workshop*, September 2010.
- [8] E. Oliveri and E. Graverini. Large GEM detector: August TB results. In *6th RD51 Collaboration meeting*, October 2010.
- [9] S. D. Pinto. A large area GEM detector: manufacturing of first large prototype. In *CMS high- η MPGD workshop*, September 2010.
- [10] S. D. Pinto, M. Alfonsi, I. Brock, G. Croci, E. David, R. de Oliveira, B.-E. Pinchasik, L. Ropelewski, F. Sauli, and M. van Stenis. A large

- area GEM detector. In *IEEE Nuclear Science Symposium Conference*, 2008.
- [11] F. Sauli. Principles of operation of multiwire proportional and drift chambers. Academic training programme lectures, CERN, 1977.